



## 저작자표시-비영리-변경금지 2.0 대한민국

이용자는 아래의 조건을 따르는 경우에 한하여 자유롭게

- 이 저작물을 복제, 배포, 전송, 전시, 공연 및 방송할 수 있습니다.

다음과 같은 조건을 따라야 합니다:



저작자표시. 귀하는 원저작자를 표시하여야 합니다.



비영리. 귀하는 이 저작물을 영리 목적으로 이용할 수 없습니다.



변경금지. 귀하는 이 저작물을 개작, 변형 또는 가공할 수 없습니다.

- 귀하는, 이 저작물의 재이용이나 배포의 경우, 이 저작물에 적용된 이용허락조건을 명확하게 나타내어야 합니다.
- 저작권자로부터 별도의 허가를 받으면 이러한 조건들은 적용되지 않습니다.

저작권법에 따른 이용자의 권리는 위의 내용에 의하여 영향을 받지 않습니다.

이것은 [이용허락규약\(Legal Code\)](#)을 이해하기 쉽게 요약한 것입니다.

[Disclaimer](#)

공학박사학위논문

나노다공성 양극산화 알루미나 기반  
25 mm<sup>2</sup> 면적의 YSZ 박막 연료전지  
구조 개발

Development of Submicron YSZ Electrolyte Fuel  
Cell Structure of 25 mm<sup>2</sup> on Nanoporous  
Anodized Alumina

2015년 8월

서울대학교 대학원

기계항공공학부

박 준 호

Development of Submicron YSZ  
Electrolyte Fuel Cell Structure of 25 mm<sup>2</sup>  
on Nanoporous Anodized Alumina

by  
Joonho Park

A Dissertation Submitted in Partial Fulfillment  
of the Requirements for the Degree of  
DOCTOR OF PHILOSOPHY

Department of Mechanical and Aerospace Engineering  
Seoul National University

August 2015

## ABSTRACT

# Development of Submicron YSZ Electrolyte Fuel Cell Structure of 25 mm<sup>2</sup> on Nanoporous Anodized Alumina

Joonho Park

Department of Mechanical and Aerospace Engineering

Seoul National University

Student Number: 2008-20746

Intermediate temperature thin-film fuel cells have received a great deal of attention as a novel fuel cell system owing to their high energy density at operating temperatures lower than 500 °C. Also, recent advances in micro/nanoscale fabrication process and analysis technology facilitated various approaches regarding the architectures of thin-film fuel cells. Meanwhile, porous templates have been suggested as supports in order to overcome the mechanical limitations of the membranes with thicknesses of only tens or hundreds of nanometers.

In terms of activation overpotential, oxygen reduction reactions

are more dominant than hydrogen oxidation reactions. Thus, many researches on thin-film fuel cells have been concentrated on the design of cathodes and the improvement of interfaces between electrolytes and cathodes rather than anodes. In the porous substrate based thin-film fuel cells, however, the anode is directly deposited on the array of nano-pores, so that the effects of the deposition conditions on the morphological properties of the electrode and eventually on the fuel cell performance can be thoroughly studied. It was revealed that the anode structure greatly affects the electrochemical reactivity and mass transfer rate by determining distribution of triple-phase boundaries (TPBs) and porosity in the electrode.

Previous researches on the porous substrate based thin-film fuel cells have greatly contributed in preventing pinhole defects in the electrolytes. Recently, it has been reported that open circuit voltages (OCVs) higher than 1 V could be achieved by applying atomic layer deposition (ALD) to fabrication of nano-thin electrolyte membranes. The yttria stabilized zirconia (YSZ) electrolyte thin-films produced by ALD reportedly shows improved electrochemical characteristics compared to those produced by traditional processes. In this study, fabrication and characterization of thin-film SOFCs supported by the porous substrates were examined in terms of electrolytes deposition techniques, which were sputtering and ALD. The results of

electrochemical evaluations showed that the fuel cell power density could be more than doubled by employing the ALD YSZ electrolyte rather than the sputtered YSZ. Moreover, it also showed that the ALD YSZ interface at cathode side could mitigate the degradation of porous Pt electrode, eventually improving the durability of the thin-film fuel cells based on the porous substrates.

The porous substrate based structures have been proposed for scale up of micro fuel cells by improving thermos-mechanical stability of the thin-films. In this study, the thin-film fuel cells with active area of  $25 \text{ mm}^2$  were successfully demonstrated. Furthermore, even though the scaling up of nano-thin electrode caused additional ohmic losses, the total power output generated by a single cell was about 25 mW, which is enhanced by  $\sim 18.5 \%$  compared to the previous study reported by Tsuchiya *et al.* (the total power of 21.1mW and the active area of  $13.5 \text{ mm}^2$ ).

This study examined the effects of the design of anode structures and the deposition technique of electrolytes on the electrochemical performance and the long-term durability in the thin-film fuel cells supported by the porous substrates.

## CONTENTS

ABSTRACT .....	I
CONTENTS .....	IV
LIST OF FIGURES .....	VII
LIST OF TABLES .....	IX
CHAPTER 1 INTRODUCTION .....	1
1.1 Motivation .....	1
1.2 Background Research: Architectures of Thin–Film SOFCs .....	5
1.2.1 Free–Standing Structure .....	5
1.2.2 Porous Substrate Based Structure .....	8
1.2.3 Scale Up of Thin–Film SOFCs .....	11
1.3 Objectives .....	13
CHAPTER 2 ENGINEERING MICROSTRUCTURE OF THIN– FILM ANODES ON NANO–POROUS SUBSTRATES .....	15
2.1 Introduction .....	15
2.2 Experimental Details .....	18
2.3 Configurations of the Fabricated Cells .....	20
2.4 Results of Electrochemical Characterizations .....	22
2.5 Morphological Analysis for the Cell Components .....	34
2.6 Conclusion .....	40

CHAPTER 3	ATOMIC LAYER DEPOSITION OF YTTRIA STABILIZED ZIRCONIA FOR ENHANCED REACTIVITY AND STABILITY OF SOLID OXIDE FUEL CELLS .....	41
3.1	Introduction .....	41
3.2	Experimental Details .....	44
3.2.1	Thin–Film Deposition .....	44
3.2.2	Cell Fabrication.....	46
3.2.3	Characterization.....	47
3.3	Results and Discussion .....	48
3.3.1	Configurations of Fabricated Cells .....	48
3.3.2	Electrochemical Reactivity of the Fuel Cells .....	50
3.3.3	Enhanced Long–Term Stability of the ALD–YSZ ..	61
3.1	Conclusion.....	72
CHAPTER 4	SCALE UP OF THIN–FILM SOLID OXIDE FUEL CELLS ON NANO–POROUS SUBSTRATES.....	73
4.1	Introduction .....	73
4.2	Experimental .....	75
4.2.1	Sample Preparation .....	75
4.2.2	Fuel Cell Test .....	78
4.3	Results and Discussion .....	79
4.3.1	Morphologies of Fabricated Cells .....	79
4.3.2	Effects of Cathode Porosity on Performance of Thin–Film Fuel Cells with Larger Active Areas.....	81
4.3.3	Improvement of Current Collection .....	86
4.4	Conclusion.....	89
CHAPTER 5	CONCLUDING REMARKS .....	90



5.1 Summary .....	90
5.2 Future Works.....	92
REFERENCES .....	94
국문 초록 .....	105

## LIST OF FIGURES

Figure 1.1 Ionic conductivities of ceramic electrolyte materials [3] .....	3
Figure 1.2 Schematics of (a) free-standing and (b) porous substrate supported structures of thin-film SOFCs.....	6
Figure 1.3 Schematic of a pinhole in an electrolyte of an AAO based thin-film SOFC.....	8
Figure 2.1 cross sectional images of the fabricated cells with different anode structures .....	21
Figure 2.2 j-V curve of the fabricated cells (a) with dense anodes deposited at 5 mTorr, and (b) with porous anodes deposited at 90 mTorr. The values next to the plots (150, 300 and 450) represent the anode thicknesses in nm of the corresponding cells [55].....	23
Figure 2.3 Electrochemical impedance spectra measured at the OCVs for the fabricated cells with dense anodes deposited at 5 mTorr. ....	25
Figure 2.4 ohmic resistances and faradaic resistances of the fabricated cells with dense anodes calculated by equivalent circuit models.....	28
Figure 2.5 Electrochemical impedance spectra measured at the OCVs for the fabricated cells with porous anodes deposited at 90 mTorr. ....	30
Figure 2.6 ohmic resistances and faradaic resistances of the fabricated cells with porous anodes calculated by equivalent circuit models.....	31
Figure 2.7 Tafel ( $\eta_{act}$ vs $\ln(j)$ ) plot based on the current density-voltage curves .....	33
Figure 2.8 Surface morphologies of the anodes on the AAO substrates .....	34

Figure 2.9 Surface morphologies of the electrolytes .....	36
Figure 2.10 Surface morphologies of the cathodes .....	39
Figure 3.1 Cross-sectional images of the fabricated cells...	48
Figure 3.2 Current density–voltage curves of the fabricated cells.....	50
Figure 3.3 Electrochemical impedance spectra of (a) the fabricated cells at 0.5 V and (b) the sputtered YSZ cell at OCV and 0.5 V, and (c) the plots magnified at high-frequencies .....	51
Figure 3.4 Topography of the electrolyte surfaces of (a) the sputtered YSZ cell, (b) the ALD YSZ cell and (c) the multilayered YSZ cell.....	55
Figure 3.5 XRD patterns of the sputtered YSZ and ALD YSZ before and after annealing .....	59
Figure 3.6 Galvanostatic measurements of the sputtered YSZ cell and the ALD YSZ cell.....	61
Figure 3.7 Current density–voltage curves of the sputtered YSZ cell before and after the galvanostatic measurement. ....	62
Figure 3.8 Electrochemical impedance spectra of the sputtered YSZ cell before and after the galvanostatic measurement .....	63
Figure 3.9 A STEM image and an EDS profile of the cathode and the electrolyte of the sputtered YSZ cell. ....	65
Figure 3.10 Morphologies of porous Pt cathode deposited on the sputtered YSZ thin film (a) before and (b) after annealing for 10 hours at 450 °C .....	68
Figure 3.11 Morphologies of porous Pt cathode deposited on the ALD YSZ thin film (a) before and (b) after annealing for 10 hours at 450 °C .....	69

Figure 3.12 Morphologies of the sputtered YSZ thin film (a) before and (b) after annealing for 10 hours at 450 °C ...	70
Figure 3.13 Topographies of the Pt cathodes on (a) the sputtered YSZ and (b) the ALD YSZ films .....	71
Figure 4.1 Schematics of (a) cell 1 and 2, and (b) cell 3 .....	77
Figure 4.2 Cross-sectional imager of the fabricated cells ...	79
Figure 4.3 Morphologies of the Pt cathodes of (a) cell1 and (b) cell 2 .....	80
Figure 4.4 Current density–voltage curves of cell 1 and 2 ..	83
Figure 4.5 Electrochemical impedance spectra of cell 1 and 2 .....	83
Figure 4.6 Sheet resistance of the Pt thin films with variance of the sputtering pressure .....	85
Figure 4.7 Current density–voltage curves of cell 2 and 3 ..	87
Figure 4.8 Electrochemical impedance spectra of cell 2 and 3 .....	87

## LIST OF TABLES

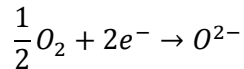
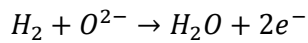
Table 1.1 Description of fuel cell types [13] .....	2
Table 2.1 Sputtering conditions for the cell components .....	19
Table 3.1 Surface properties calculated from the AFM measurements .....	56
Table 3.2 XRD results of YSZ thin films .....	57
Table 4.1 Sputtering conditions of the electrodes and the current collector .....	76

## CHAPTER 1 INTRODUCTION

### 1.1 Motivation

A fuel cell directly produces electricity from electrochemical reactions without complex and inefficient conversions among mechanical, heat and chemical energies [1]–[12]. In a fuel cell, the electrochemical reactions can be divided into two electrochemical reactions: hydrogen oxidation reaction (HOR) and oxygen reduction reaction (ORR). As water is the only byproduct of these reactions, fuel cells are known to be a highly efficient and eco-friendly power source.

In general, fuel cells are classified by their electrolytes, as shown in Table 1.1, which are polymer membrane fuel cell (PEMFC), phosphoric acid fuel cell (PAFC), alkaline fuel cell (AFC), molten carbonate fuel cell (MCFC) and solid oxide fuel cell (SOFC) [13]. Among these electrolytes, SOFCs use thin ceramic membranes as the electrolyte and oxygen ions transfer charge through the electrolyte membranes [14]. In SOFCs, the basic electrochemical reactions are as follows:



SOFCs are widely used in stationary systems owing to their high efficiency and fuel flexibility.

Table 1.1 Description of fuel cell types [13]

	PEMFC	PAFC	AFC	MCFC	SOFC
Electrolyte	Polymer membrane	Liquid $\text{H}_3\text{PO}_4$ (immobilized)	Liquid KOH (immobilized)	Molten carbonate	Ceramic
Charge carrier	$\text{H}^+$	$\text{H}^+$	$\text{OH}^-$	$\text{CO}_3^{2-}$	$\text{O}^{2-}$
Operating temperature	80 °C	200 °C	60-200 °C	650 °C	600-1000 °C
Catalyst	Platinum	Platinum	Platinum	Nickel	Perovskite (ceramic)
Cell components	Carbon based	Carbon based	Carbon based	Stainless based	Ceramic Based
Fuel compatibility	$\text{H}_2$ , methanol	$\text{H}_2$	$\text{H}_2$	$\text{H}_2$ , $\text{CH}_4$	$\text{H}_2$ , $\text{CH}_4$ , CO

The temperature dependence of the ion conductivity in most ceramic electrolyte materials can be explained by the Arrhenius behaviors, as shown in Figure 1.1 [3]. Thus, traditional SOFCs typically operate at approximately 600–1000 °C to obtain high ionic conductivity of the ceramic electrolyte represented by yttria stabilized zirconia (YSZ) [15]–[19]. However, such high operating temperature may have difficulties as thermal stress and severe degradation. Moreover, it requires special materials

for gas sealing and heat maintenance, leading to significant challenges in design and expense. Therefore, many researchers have endeavored to reduce the operating temperature of SOFCs [17]–[30].

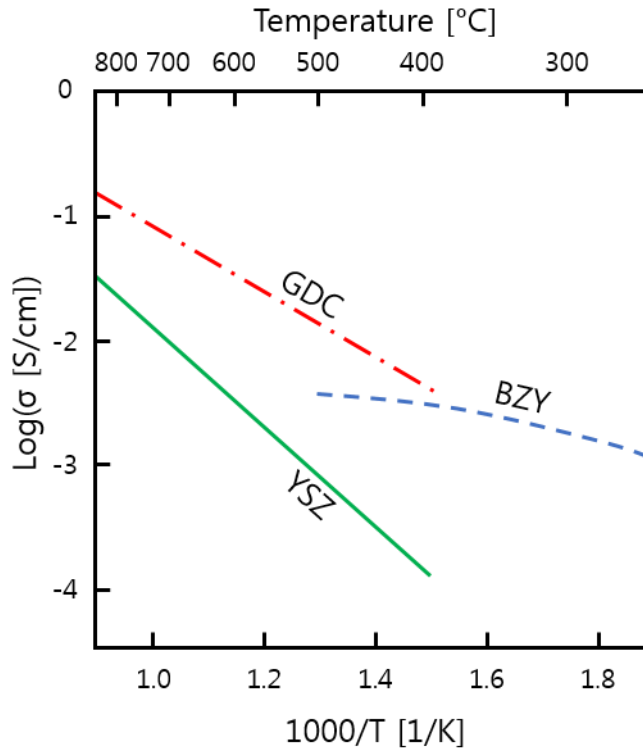


Figure 1.1 Ionic conductivities of ceramic electrolyte materials [3]

To compensate the higher ohmic losses owing to the low ionic conductivity of solid oxide electrolyte at lower temperatures, two kinds of approaches have been investigated: developing

new electrolyte materials which present higher ionic conductivity than YSZ at low temperatures, and reducing the electrolyte thickness to shorten the ionic path [30]–[37]. Although gadolinium doped ceria (GDC) and yttrium doped barium zirconate (BZY) show higher conductivity than YSZ, as shown in Figure 1.1, YSZ is known as the most stable material in both highly reducing environment of the anode side and extremely oxidizing atmosphere of the cathode side [13], [14]. Area-specific resistance (ASR), which is also known as area-normalized resistance, is defined as:

$$ASR = \frac{L}{\sigma}$$

where  $L$  is the length and  $\sigma$  is the conductivity. Therefore, to reduce the resistance, it is necessary to make the electrolyte membranes as thin as possible. For this reason, extensive researches have been carried out to demonstrate thin-film SOFCs operated at lower temperatures (<500 °C).



## 1.2 Background Research: Architectures of Thin-Film SOFCs

### 1.2.1 Free-Standing Structure

The architectures for thin-film SOFCs can be classified under two groups: free-standing and porous substrate-supported structures. Figure 1.2 (a) and (b) represent the schematic of free-standing and porous substrate based structure, respectively. Applying microelectromechanical system (MEMS) processing allows the fabrication of free-standing SOFC electrolytes in sub-micro scale [38]. In this research, 1.05~1.10 V of open circuit voltage (OCV) and 130 mW/cm<sup>2</sup> of peak power density at 350 °C were reported. More enhanced fuel cell performance was reported by a study about free-standing thin-film SOFC with 60 nm thick electrolyte formed by ALD (atomic layer deposition) process representing 270 mW/cm<sup>2</sup> of peak power density [39]. In these researches, the enhanced charge transfer kinetics on the nano-crystalline YSZ was observed. In addition, it was suspected that the higher overall performance of the ALD YSZ fuel cell than one containing the RF sputtered nano-crystalline membrane could be related to the nano-grain morphology of ALD YSZ films [40].

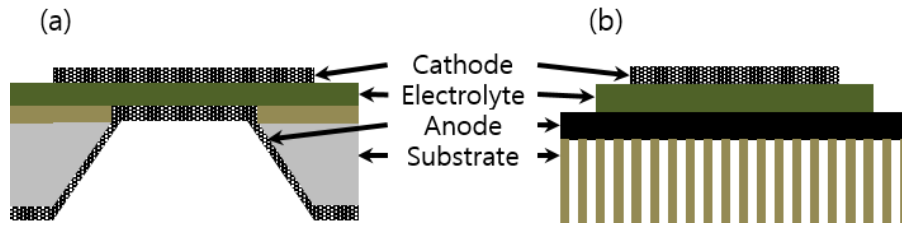


Figure 1.2 Schematics of (a) free-standing and (b) porous substrate supported structures of thin-film SOFCs

Despite high power densities of thin film fuel cells based on free standing structure, the absolute power output is too low for practical use. This is because the electrochemically active area is too small and the surface utilization is inefficient due to crystallographic constraints on wet etching of (100) silicon wafers. To increase the active area of free standing thin-film fuel cells, a patterned membrane was employed instead of a flat one. For this purpose, the corrugated electrolyte structure was developed by cup-shaped patterning via deep reactive ion etching (DRIE) [41]. The peak power density of the fuel cell with 70 nm thick corrugated membrane and DC sputtered 120 nm thick electrodes was  $677 \text{ mW/cm}^2$ , which is 1.9 times that of the flat membrane at  $400^\circ\text{C}$ . The sizes of both flat and corrugated membrane in this result were  $600 \mu\text{m} \times 600 \mu\text{m}$ . This result shows that the performance of free-standing

structured thin-film SOFCs can be improved by enlarging the effective active area by MEMS patterning techniques.

The three-dimensionally patterned free standing membrane was produced by applying nano-sphere lithography (NSL) to increase the active area and improve the corrugated structure [42]. The monolayer of Silica nanoparticles on the silicon substrate was formed via Langmuir-Blodgett method to fabricate metal mask and then, the three-dimensional nanostructure surface on the substrate was achieved by several etching steps. The thicknesses of sputtered platinum electrodes and ALD YSZ electrolyte were 80 nm and 60 nm, respectively. The peak power density of the nano-patterend cell was 1.34 W/cm<sup>2</sup> at 500 °C with a projected area of 10<sup>-4</sup> cm<sup>2</sup>, which means that the total power output was 134 μW. The peak power density of the unpatterned cell with the same projected area was 900 mW/cm<sup>2</sup>.

### 1.2.2 Porous Substrate Based Structure

Another approach to develop thin-film SOFCs is applying certain porous substrates in order to provide mechanical stability and effective gas delivery at the same time [34], [43]–[45]. Additionally, the electrode structure sandwiched by the porous template and the electrolyte is expected to mitigate the degradation of the fuel cell. Moreover, it is relatively easy to fabricate cells based on the porous substrates compared to the free-standing architectures. This is because the former does not necessarily require complicated steps as photolithography and chemical etching.

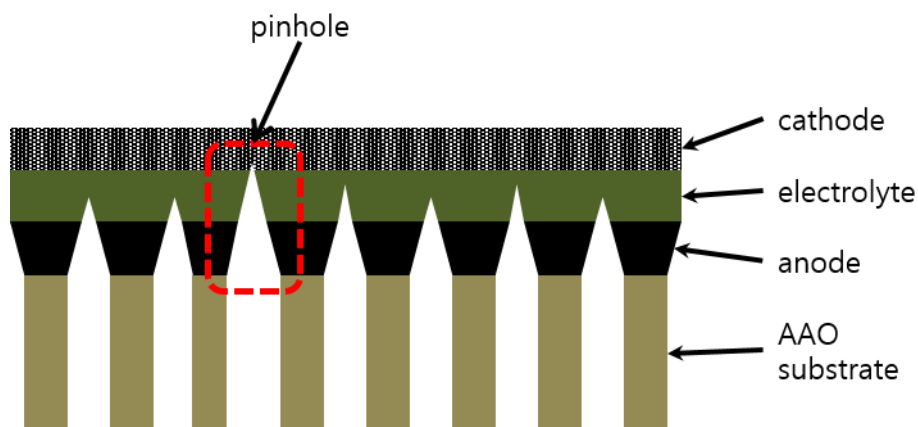


Figure 1.3 Schematic of a pinhole in an electrolyte of an AAO based thin-film SOFC

However, the thin-film SOFCs supported by porous substrates has an inherent pinhole problem because of the structural property of the substrate surfaces, as shown in Figure 1.3. The porous structure of the substrate may cause selective nucleation and grain growth, leading to propagation of pinholes and voids [46]. As these defects can result in electrical shortage or gas leakage, it is crucial to appropriately prevent them. Accordingly, some of the previous studies were able to apply ALD layers on the deposition of the electrolyte via physical vapor deposition methods (PVD) such as sputtering and pulsed laser deposition (PLD) technique, so that the membrane becomes dense enough to clog the defects [47], [48].

Kwon *et al.* designed various self-supported and anodic aluminum oxide (AAO) supported cell structures and measured their OCVs to examine the pinhole problem which is one of the most critical obstacles of the porous substrate supported fuel cells [46]. They observed propagation of the pinholes and voids, and demonstrated AAO supported micro SOFCs with ALD modified electrolyte layers. To clog the defects in PLD YSZ layer on the electrode layer,  $\text{Al}_2\text{O}_3$  layer was deposited via ALD on the surface and removed by RIE to expose the first YSZ layer followed by deposition of second YSZ layer. The OCV values that were measured from the ALD-modified cells

increased when compared to the unmodified cells with same total thicknesses. Maximum power densities of 30, 110, and 350 mW/cm<sup>2</sup> were obtained at 400, 450, and 500 °C from the fuel cell with 900 nm thick ALD-modified YSZ. This result shows that the fuel cell performance can be improved by eliminating the pinholes in the electrolyte layer.

It has been reported that the combination of a sputtered electrolyte layers and thin ALD YSZ layers can effectively prevent the pinholes [47], [48]. Ji *et al.* have successfully formulated a nano-porous substrate supported thin-film fuel cell, with a bilayered electrolyte composed of a sputtered GDC layer and an ALD YSZ layer [48]. The GDC is known as an electrolyte material, which has excellent oxygen ion conductivity even at low temperatures [15], [18], [35]. Meanwhile, it also has the tendency of being easily reduced at low oxygen partial pressures, which makes it more conductive for electrons than ions [15]. It was shown that the thin ALD YSZ protective layer between the anode and the GDC electrolyte could prevent the reduction of ceria as well as the pinhole propagation [35], [48].

### 1.2.3 Scale Up of Thin-Film SOFCs

Most researches on free-standing SOFCs have demonstrated the fuel cells with lateral dimensions of micrometer scale. Thus, to increase total power output for practical use, comprehensive studies about scaling up of the active area are required. However, scaling up free-standing structures poses a great challenge because large-area membranes less than  $\sim 100$  nm are susceptible to mechanical failures.

A research about strengthening the large area of thin-film solid oxide fuel cell membrane was recently reported. [49]. In this study, a 200 nm thick free-standing fuel cell comprised of platinum anode, YSZ electrolyte and LSCF cathode was fabricated and supported by plated nickel grid. However, the OCV and peak power density are only 0.2 V and  $1 \text{ mW/cm}^2$  at  $500^\circ\text{C}$ .

Tsuchiya *et al.* produced and characterized a free standing thin-film SOFC with  $13.5 \text{ mm}^2$  of active area applying about  $1.5 \text{ }\mu\text{m}$  grid layer on the cathode via additional photolithography process [50]. The MEA of the fuel cell was composed of 30 nm thick porous platinum anode layer, 54 nm thick RF sputtered YSZ electrolyte, and 47 nm thick RF sputtered LSCF cathode layer. They reported  $\sim 0.75$  V of OCV and  $155 \text{ mW/cm}^2$  of peak

power density, thus, approximately 21 mW of the total power output from a single fuel cell chip. However, even though the metallic grid had successfully functioned as mechanical supports, there were a few cases of buckling of the membranes. Although the feasibility of scaling the thin-film up SOFCs by using porous templates has been reported in previous studies, the active areas of the fabricated cells in those studies were less than only 1 mm<sup>2</sup> [48], [51]–[53]. Therefore, it is necessary to demonstrate thin-film SOFCs with active areas larger than 1 mm<sup>2</sup> based on the AAO template.



### 1.3 Objectives

This study focused on the development of the thin-film SOFC supported by the nano-porous substrate for reliable scale up. First, the microstructure of the anodes on nano-porous templates was investigated to reveal the effects of the porosity and the thickness of anode layers on the electrochemical properties in AAO based thin-film SOFCs. In thin-film SOFCs supported by the porous substrates, a single cell is fabricated by a sequential deposition of anode, electrolyte and cathode. Thus, it requires a thorough examination on the structural effects of the anode layer, which is the base structure of the membrane electrode assembly (MEA).

Constructing the electrolyte is a key factor in the fabrication of thin-film SOFCs because any defects in the electrolyte would cause gas leakage or electrical shortage, eventually resulting in a failure of operation in fuel cells. In addition, in the AAO based thin-film SOFCs, surface properties of the electrolyte greatly affect the formation of the cathode and interfacial kinetics of ORR. In this study, thin-film SOFCs supported by AAO substrates were fabricated with YSZ electrolytes deposited by different thin film techniques to examine the effects of the electrolyte deposition method on electrochemical reactivity and long-term stability.

Lastly, thin-film SOFCs based on AAO substrates were successfully demonstrated with active areas as large as 25 mm<sup>2</sup>. The best power density of the cells with active area of 25 mm<sup>2</sup> was approximately 100 mW/cm<sup>2</sup> at 500 °C, which indicates the total power output of the single cell was about 25 mW. It is higher by ~18.5 % compared to the total power output reported by Tsuchiya *et al.* [50]. Moreover, the effects of the cathode morphology on ohmic and faradaic resistances of the fuel cells were assessed by characterizing the fuel cells with different cathode morphologies. Finally, it is suggested that optimizing current collections in the thin-film electrodes with extremely high aspect ratio is a crucial factor to enhance the overall electrochemical performance of the fuel cells with larger active areas.

## CHAPTER 2      ENGINEERING MICROSTRUCTURE OF THIN-FILM ANODES ON NANO-POROUS SUBSTRATES

### 2.1 Introduction

In consideration of the thermomechanical stability, nano-porous templates were suggested as substrates to support thin film fuel cells for their higher reliability as well as efficient gas delivery. It has been demonstrated that in cases where thin films are supported by nano-porous AAO templates, their electrical and microstructural degradation could be significantly mitigated even at elevated temperatures [34], [45]–[48], [54]–[56]. In most of early researches about thin-film fuel cells with the AAO templates, the open circuit voltages (OCVs) were relatively low because of the pin-hole defects in the thin electrolyte inherently caused by porous structure of the substrates [46]. Extensive efforts therefore have been devoted to producing defect-free electrolyte layers with thickness of sub-micrometer on the AAO. As a result, the thin-film SOFCs on the porous substrates have been successfully demonstrated without any gas leakage, with the assistance of bi-layered electrolytes and modified electrolytes with various thin film deposition techniques [34], [45]–[48], [54]–[56].

To date, in most studies on the thin film SOFCs supported by the AAO, the anode layers have been deposited to form a dense structure because the dense anode has been regarded as helpful in preventing the pin-hole problems. Moreover, it has been reported that there was no need for the anodes to form porous microstructures because the pores of the substrate were not fully clogged by thin-film anodes in spite of their dense structures [34].

However, the porous electrode structure is known to be beneficial for mass transport which is one of the main factors to determine the fuel cell performance [13], [14]. Additionally, in terms of the active area at the anode side, the thin film structure based on the AAO can have disadvantages compared to the anode-supported and free-standing structures. Thus, more porous anodes may be favorable to the thin-film SOFC supported by the AAO and the properties of the anode microstructures should be further investigated in order to optimize the performance of the cell.

In this study, the thin-film SOFCs supported by the AAO with the porous anodes were demonstrated. To the extent of our knowledge, this study is the first to examine the anode microstructures for the AAO-based thin-film fuel cell structures. In addition, various anode microstructures were examined to find out the key effects of the porosity and the

thickness of anode thin films on the electrochemical performance in this structure of fuel cell.

## 2.2 Experimental Details

A commercial AAO (Synkera Technology Inc.) with a thickness of 100  $\mu\text{m}$  and a pore diameter of 80 nm was used as a template to support the thin-film SOFCs with thicknesses of hundreds of nanometers. Platinum thin films were sputtered on the AAO template with power of 200 W for the anode layers. To fabricate a set of different anode layers, we varied the sputtering time and the argon gas pressure in the sputter chamber. The chamber pressure was regulated to 5 and 90 mTorr, and the sputtering time was also controlled to achieve the platinum thin films with different thicknesses of 150, 300 and 450 nm each at 5 and 90 mTorr. Subsequently, YSZ electrolyte and porous platinum cathode were sputtered on the anodes under identical sputtering conditions for all cells to investigate the effects of the anode structure on the fuel cell performance, aside from the effects resulting from electrolytes and cathodes. The YSZ electrolytes with a thickness of approximately 500 nm were sputtered from an  $\text{Y}_{16}\text{Zr}_{84}$  alloy target at 200 W. The YSZ deposition was conducted at 5 mTorr of  $\text{Ar}/\text{O}_2$  atmosphere and room temperature. A porous Pt cathode with a thickness of 150 nm was deposited by DC sputtering at 100 W at room temperature with an Ar pressure of 90 mTorr. A shadow mask was used to produce the active

area of 1 mm<sup>2</sup> [48]. Polarization characteristics of the fabricated cells were measured by a commercial analytical interface Solatron 1260/1287 at 500 °C. The anode side was fed by 100 sccm of dry hydrogen through the AAO pores, while the cathode side was exposed to oxygen in ambient air during the fuel cell test. The field emission secondary electron microscope (FE–SEM: Supra 40, Carl Zeiss) was utilized to examine the surface morphologies of the anode, the YSZ electrolyte and the cathode of the fuel cells. The focused ion beam and scanning electron microscope (FIB–SEM: Quanta 3D FEG, FEI Company) were utilized to observe the cross-sectional images of the fabricated fuel cells.

Table 2.1 Sputtering conditions for the cell components

	Target material	Background Gas	Sputtering power [W]	pressure [mTorr]	Substrate temperature
Anode	Pt	Ar	200	5~90	RT
Electrolyte	Y <sub>16</sub> Zr <sub>84</sub>	Ar/O <sub>2</sub>	200	5	RT
Cathode	Pt	Ar	100	90	RT

## 2.3 Configurations of the Fabricated Cells

Figure 2.1 represents cross sectional images of the fabricated thin-film SOFCs on AAO substrates. In all cells, the deposition condition of the electrolyte and the cathode were identical; whereas the structure of the anodes was differently formed. The thickness and the porosity of the anodes were controlled by varying the deposition time and the argon pressure in the sputter chamber.

As shown in Figure 2.1, the cells with the platinum anodes which were sputtered at 5 mTorr of argon pressure showed relatively dense structures. On the contrary, the cells with the anodes deposited at 90 mTorr showed more porous cross sectional structures. We fabricated three cells with 150, 300 and 450 nm thick anodes which were sputtered at 5 mTorr. Moreover, we fabricated another set of cells with 150, 300, and 450 nm thick anodes sputtered at 90 mTorr. Finally, these six cells were examined to discover how the difference in the porosity and the thickness of the anodes affects the fuel cell performance.



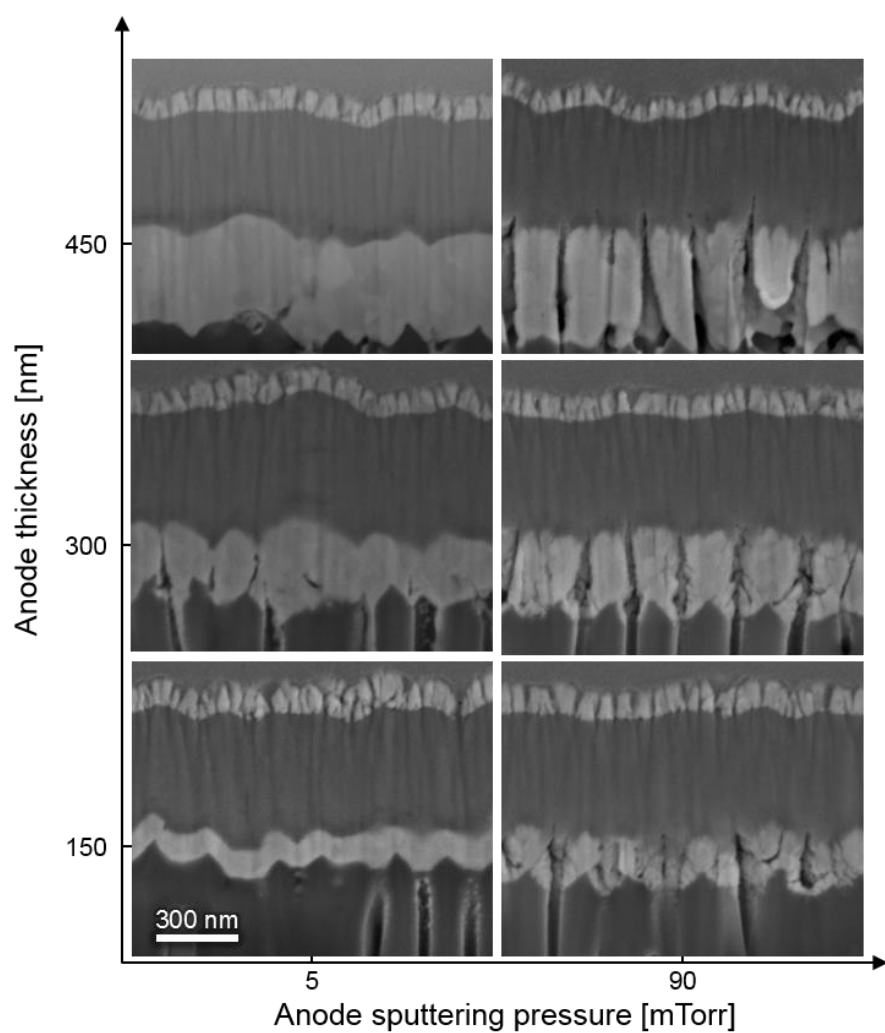


Figure 2.1 cross sectional images of the fabricated cells with different anode structures

## 2.4 Results of Electrochemical Characterizations

In Figure 2.2, the current–voltage curves of fabricated cells at 500 °C are depicted. The open circuit voltage (OCV) values for all cells were comparable, which had values between 1–1.1 V. The measured OCV values were close to the theoretically expected values at given conditions from the Nernst equation, 1.2 V, regardless of the anode structures [13]. These OCV values indicate that the electrolytes were dense enough to be free from pin–hole defects such as severe gas leakage or electrical shortage, even though the cells were fabricated on nano–porous substrates. Previous studies using AAO substrates, however, have shown that YSZ electrolytes with a thickness of several hundred nanometers sputtered on AAO templates were likely to have serious pin–hole defects [46]. This is the reason why dense anodes were primarily used to mitigate the inherent pin–hole problems in many previous researches of thin–film fuel cells supported by porous substrates. In this study, however, non–defective, nanometers–thick electrolytes were successfully produced on porous anodes. The fabrication of the AAO–based thin–film fuel cells even on the 150 nm thick, highly porous anode layer was successfully demonstrated, as shown in Figure 2.1 and

Figure 2.2 (b).

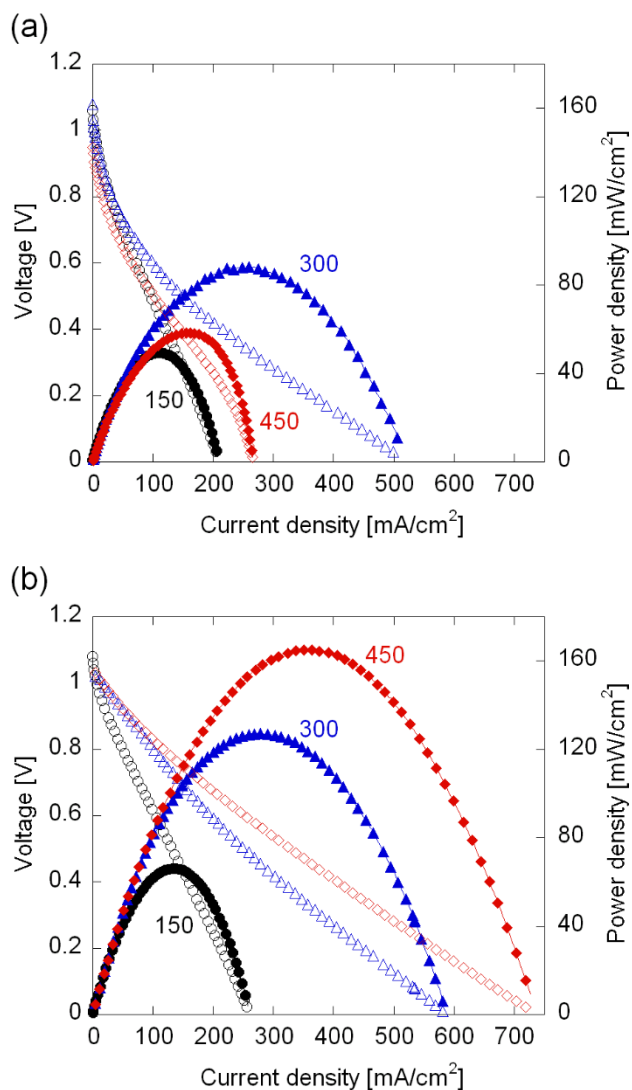


Figure 2.2 j-V curves of the fabricated cells (a) with dense anodes deposited at 5 mTorr, and (b) with porous anodes deposited at 90 mTorr. The values next to the plots represent the anode thicknesses in nm of the corresponding cells [55].

Moreover, with our simple fabrication of thin-film fuel cells, composed of sequential depositions by sputtering on the anode, the electrolyte and the cathode, we were able to fabricate thin-film SOFCs in no less than 1  $\mu\text{m}$ .

Figure 2.2 (a) shows the  $j$ - $V$  curves of the cells sputtered with 5 mTorr-sputtered anodes. According to the plots, the peak power densities were 49, 88 and 58  $\text{mW}/\text{cm}^2$  for the cells with the anodes of 150, 300 and 450 nm thickness, respectively. The maximum power density of the fuel cell rose by 80 % as the dense anode's thickness increased from 150 nm to 300 nm; however, it rather dropped by 34 % as the thickness further increased from 300 nm to 450 nm. Moreover, in the 450 nm thick dense anode cell, a drastic voltage drop was observed at the high current region of the polarization curve. It means that the depletion of the reactant concentration at the electrode/electrolyte interface was severe in this particular cell. The  $j$ - $V$  curves of the cells with the porous anodes of different thicknesses which were sputtered at 90 mTorr of chamber pressure are shown in Figure 2.2 (b). The peak power densities of the cells with the porous anode thickness of 150, 300 and 450 nm were 65, 108 and 165  $\text{mW}/\text{cm}^2$ , respectively.

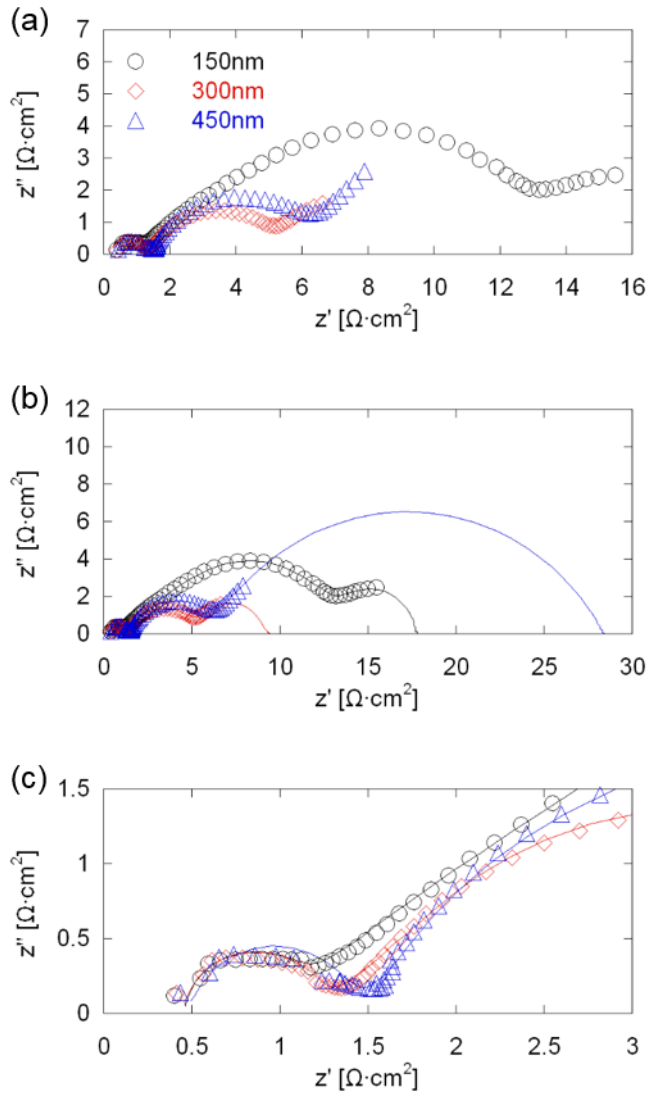


Figure 2.3 Electrochemical impedance spectra measured at the OCVs for the fabricated cells with dense anodes deposited at 5 mTorr.

In contrast with the dense anode cells, the performance of the porous anode cells steadily increased along with the increase of

the anodes' thickness. Compared to the  $j$ - $V$  curves of the porous anode cells in Figure 2.2 (b), the remarkable voltage drops at lower current densities were observed in the curves of the dense anode cells in Figure 2.2 (a).

Figure 2.3 (a) shows the electrochemical impedance spectra of the fabricated cells whose anodes were deposited at 5 mTorr. The EIS results were measured at 500 °C under the OCVs. AC perturbation of 30 mV was applied at frequencies between 2 and  $2 \times 10^6$  Hz. Figure 2.3 (b) shows Nyquist plots fitted by equivalent circuit fuel cell models. The data were fitted by a least-squares fitting procedure (Z-plot, Scribner Associate, Inc.). The complex (real and imaginary) data were fitted with data weighting given by the calculated modulus of each point [57]. The each plot in Figure 2.3 (a) contains the ohmic resistance and three arcs, so the equivalent circuits consisted of four series elements: one resistance element and three elements comprised of a parallel resistor and a constant-phase element (CPE). A CPE is used to model an imperfect capacitor to compensate for non-homogeneity in the system. As shown in Figure 2.3 (c), high-frequency intercepts of the three plots are almost identical, which means that the ohmic resistances of the three cells are very close. As represented in Figure 2.4, the calculated ohmic resistances were about 0.44 and 0.42  $\Omega \cdot \text{cm}^2$

for the cells with the anodes of 150 and 300 nm thickness, respectively. The high-frequency region in the measured plot of the 450 nm anode cell was a little unstable to be fitted by the circuit model. Thus, the ohmic resistance value of the cell with 450 nm-thick anode was fixed to  $0.42423 \, \Omega \cdot \text{cm}^2$  which is the values of the 300 nm anode cell. In general, the ohmic resistance of SOFCs is dominated by conduction of oxide ions through the electrolyte [13]. The thicknesses of the YSZ electrolytes of the three cells are identical, so the almost same ohmic resistance values are quite reasonable. Moreover, the magnitudes of the first arcs of the plots are quite similar. High-frequency arcs of impedance spectra are known to come from the electrolyte such as the ion diffusion into the grains on the electrolyte surface [58]. Therefore, the similar magnitude and shape of the high-frequency arcs in the spectra confirm that the YSZ electrolytes of the three cells were deposited under identical conditions. On the other hand, the magnitude of the low-frequency semicircles in Figure 2.3 (a) and (b) depends on the anode thickness of the cells. As shown in Figure 2.3 (b), the low-frequency semicircles were fitted by the equivalent circuit models and the complex values at lower frequencies than 2 Hz were extrapolated by using fitting results. From the predicted low-frequency intercepts and the ohmic resistances (the high-frequency intercepts), the faradaic resistance values

were calculated (Figure 2.4). The computed faradaic resistances were approximately 17.36, 9.04 and 27.96  $\Omega \cdot \text{cm}^2$  for the cells with the anodes of 150, 300 and 450 nm thickness, respectively. As thickness of the anodes deposited at 5 mTorr increased from 150 nm to 300 nm, the faradaic resistance decreased by about 48 %. However, the faradaic resistance of the cell with 450 nm thickness was about three times larger than one of the cell with 300 nm-thick anode.

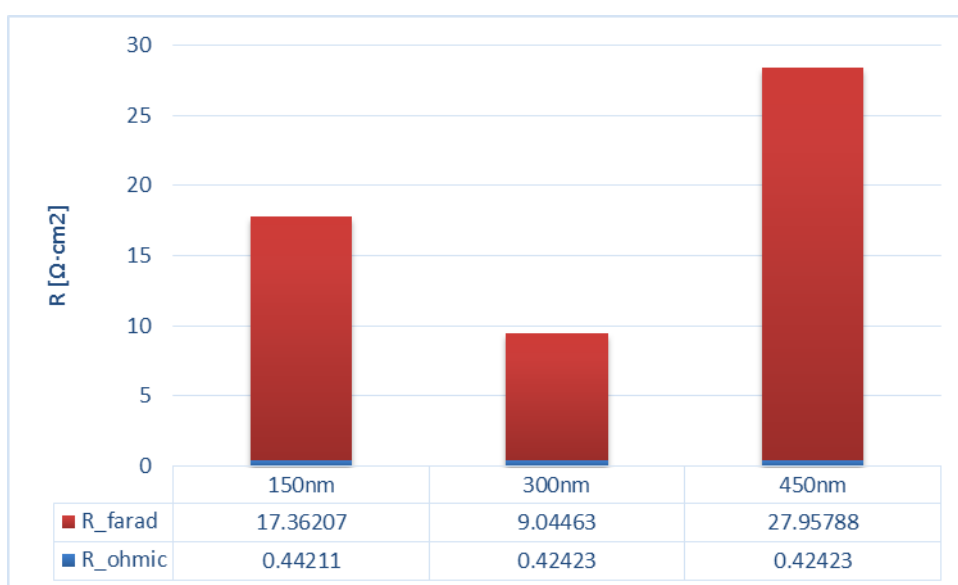


Figure 2.4 ohmic resistances and faradaic resistances of the fabricated cells with dense anodes calculated by equivalent circuit models

Figure 2.5 (a) demonstrates the electrochemical impedance



spectra of the fabricated cells whose anodes were deposited at 90 mTorr. Figure 2.5 (b) shows the fitting results and Figure 2.5 (c) depicts the detailed behaviors at high-frequencies. The ohmic resistance and the faradaic resistance values which were calculated by the equivalent circuit model are represented in Figure 2.6. The ohmic resistance values of the cell with the porous anodes of 150, 300 and 450 nm thickness were approximately 0.65, 0.60 and 0.51  $\Omega \cdot \text{cm}^2$ , respectively, while the faradaic resistance values were evaluated as about 10.78, 4.10 and 3.58  $\Omega \cdot \text{cm}^2$ . As the porous anode's thickness increased, the ohmic resistance slightly decreased. However, the difference in the ohmic resistance was minor compared to the variation in the faradaic resistance. The faradaic resistance dropped by approximately 62 % as the anode thickness increased from 150 nm to 300 nm while it decreased by only 13 % as the anode thickness increased from 300 nm to 450 nm. As shown in Figure 2.5, the high-frequency semicircles of the porous anode cells have similar magnitudes. It indicates that the high-frequency impedance behaviors originated in the bulk grains and the grain boundaries on the YSZ interfaces [58]. Thus, the tendency that the thicker anode cell showed the smaller faradaic resistance was dominated by the difference in the electrode processes, which were represented by the low-

frequency arcs in the Nyquist plots.

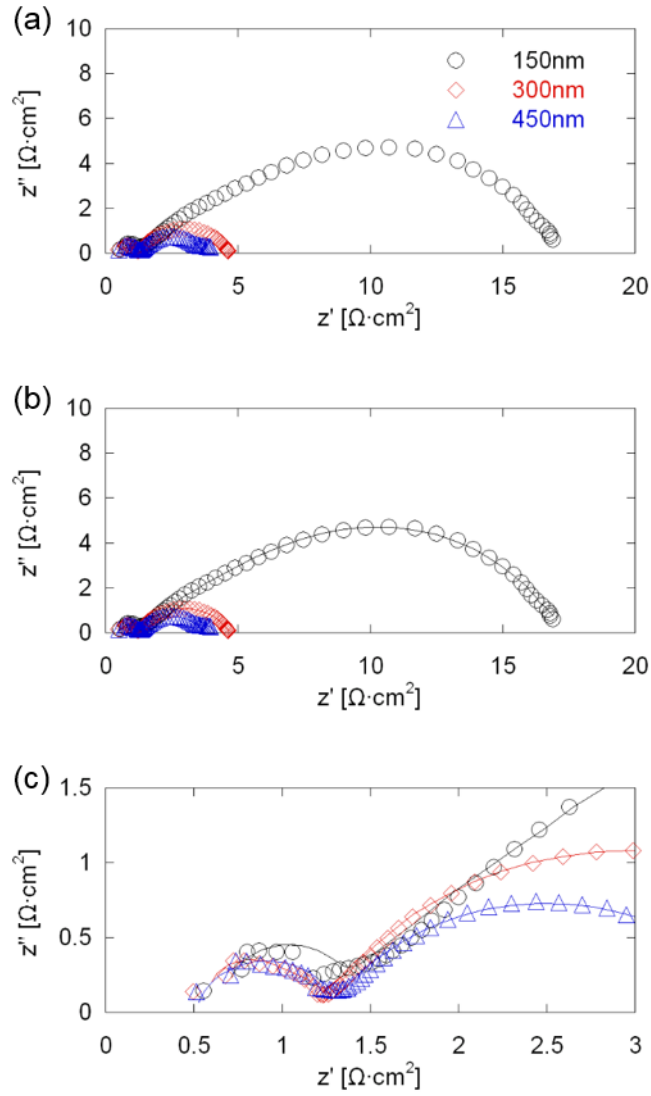


Figure 2.5 Electrochemical impedance spectra measured at the OCVs for the fabricated cells with porous anodes deposited at 90 mTorr.

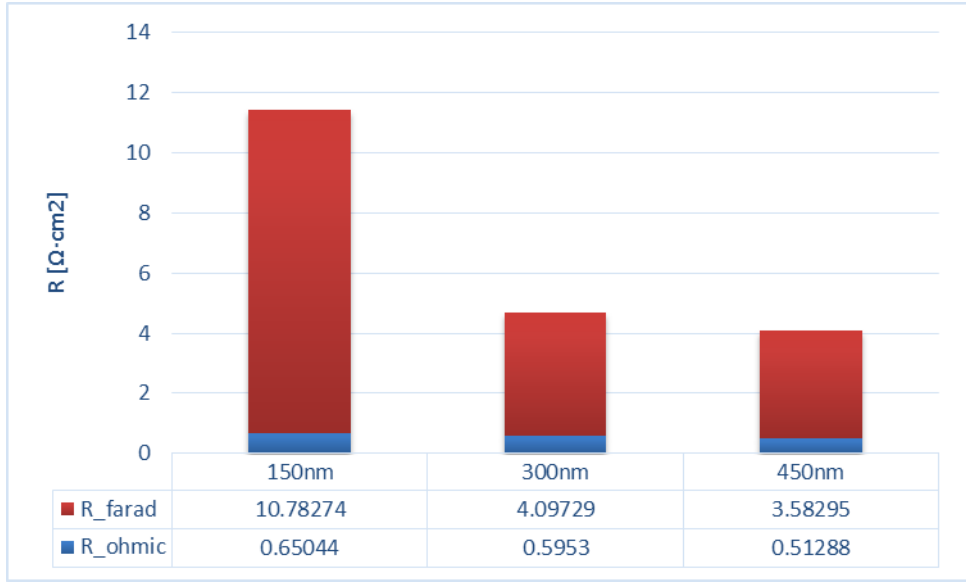


Figure 2.6 ohmic resistances and faradaic resistances of the fabricated cells with porous anodes calculated by equivalent circuit models

The electrochemical characteristic of the cells with the porous anodes is further investigated by Tafel analysis. The voltage output of a fuel cell could be written by starting with the thermodynamically predicted voltage and then subtracting the various overvoltage losses. Excluding mass transport overpotential term, the resulting fuel cell output voltage can be described as [13]:

$$V_{cell} = V_{OCV} - \eta_{act} - jASR_{ohmic}$$

where  $V_{OCV}$  is the Nernstian OCV,  $\eta_{act}$  is the activation losses

due to reaction kinetics,  $j$  is the current density, and  $ASR_{ohmic}$  is the electrolyte area specific resistance. When  $\eta_{act}$  is larger than the exchange current density ( $j_0$ ), the relation between the activation overpotential and the current density can be described by the following Tafel equation [13], [59], [60]:

$$\eta_{act} = -\frac{RT}{\alpha nF} \ln j_0 + \frac{RT}{\alpha nF} \ln j$$

where  $\alpha$  is the charge-transfer coefficient,  $j$  is the generated current density, and  $R$ ,  $T$ , and  $F$  represent the gas constant, temperature, and the Faraday constant, respectively. Figure 2.7 shows the Tafel plot ( $\eta_{act}$  vs  $\ln(j)$ ) obtained from the current density-voltage curves shown in Figure 2.2 (b).

The exchange current densities ( $j_0$ ) of the cells with the porous anode of 150, 300 and 450 nm thickness were about 9.7, 38.0, 36.1 mA/cm<sup>2</sup>, respectively. The slopes of the three plots were approximately 6.06, 5.10 and 6.09 for the cells with the 150, 300 and 450 nm-anodes, respectively. Thus, the charge-transfer coefficient values were evaluated as 0.20, 0.17 and 0.20 for each cell.

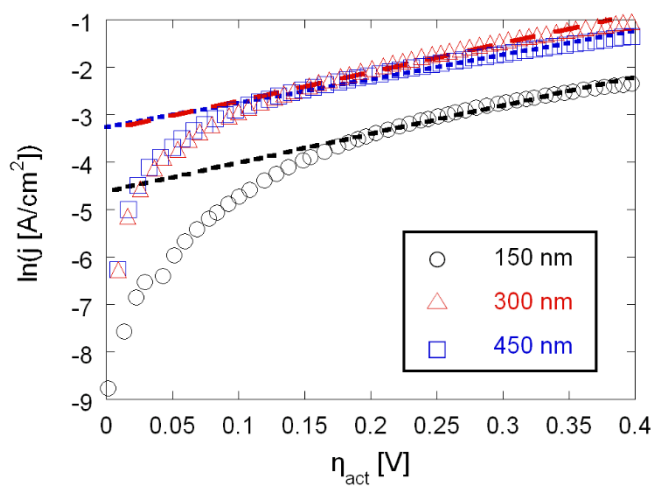


Figure 2.7 Tafel ( $\eta_{act}$  vs  $\ln(j)$ ) plot based on the current density–voltage curves

## 2.5 Morphological Analysis for the Cell Components

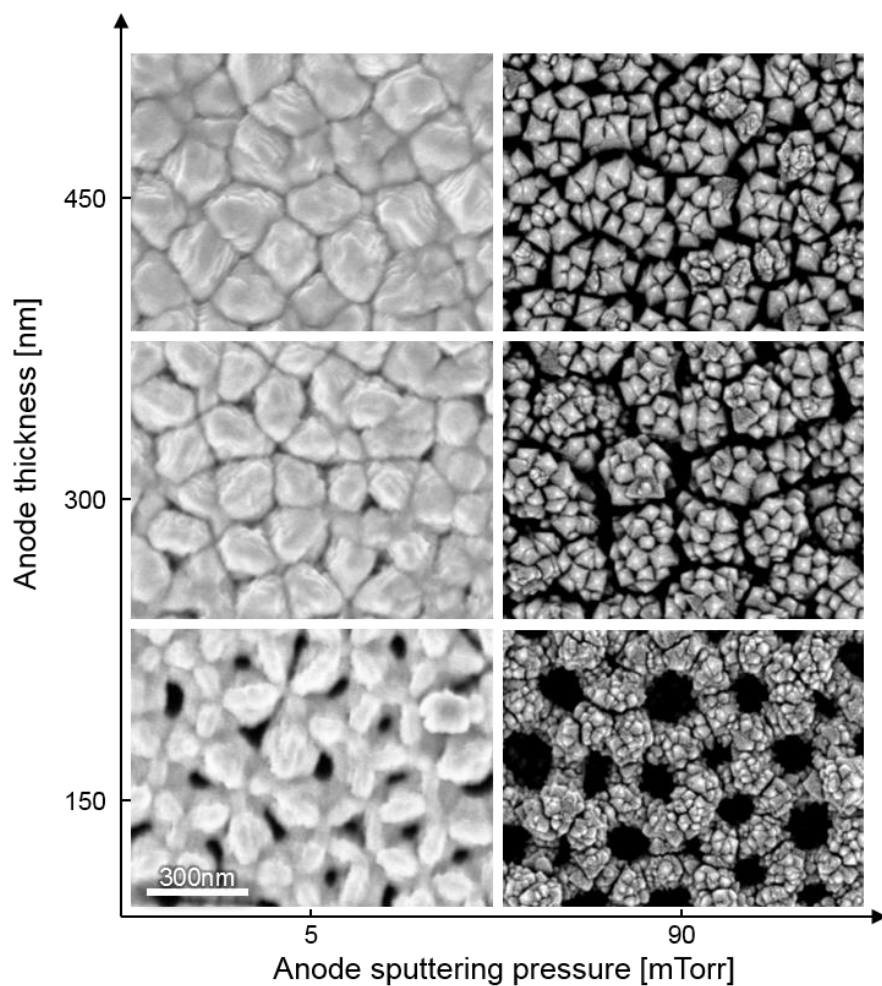


Figure 2.8 Surface morphologies of the anodes on the AAO substrates

To investigate the reason of the difference in the electrochemical performance, morphologies of surfaces on the anode, the electrolyte and the cathode layers were examined by

FE–SEM images, as respectively shown in Figure 2.8, Figure 2.9 and Figure 2.10. The morphologies of the anode surfaces were fairly different from one another as shown in Figure 2.8, while the electrolyte and cathode layers showed no noticeable difference in the surface morphology as shown in Figure 2.9 and Figure 2.10. Consequently, the formation of the electrolyte/cathode interface and the cathode morphology do not seem to be significantly influenced by the different anode structures. Thus, it can be concluded that the contrasting electrochemical behaviors among the fabricated cells shown in Figure 2.2 may come from the difference in the anode structures.

The performance of the SOFCs is known to be evaluated by numerical approximations to a standard polarization model including activation, ohmic and concentration losses [13]. Considering the ionic charge transport in electrolytes tends to be more sluggish than the electronic charge transport in electrodes, the ohmic resistance is heavily relied on the ionic contribution. Therefore, the difference among the ohmic resistances in every cell is negligible, because the microstructures of the surfaces and the cross–sections of the electrolytes were highly similar as shown in Figure 2.1 and Figure 2.9.

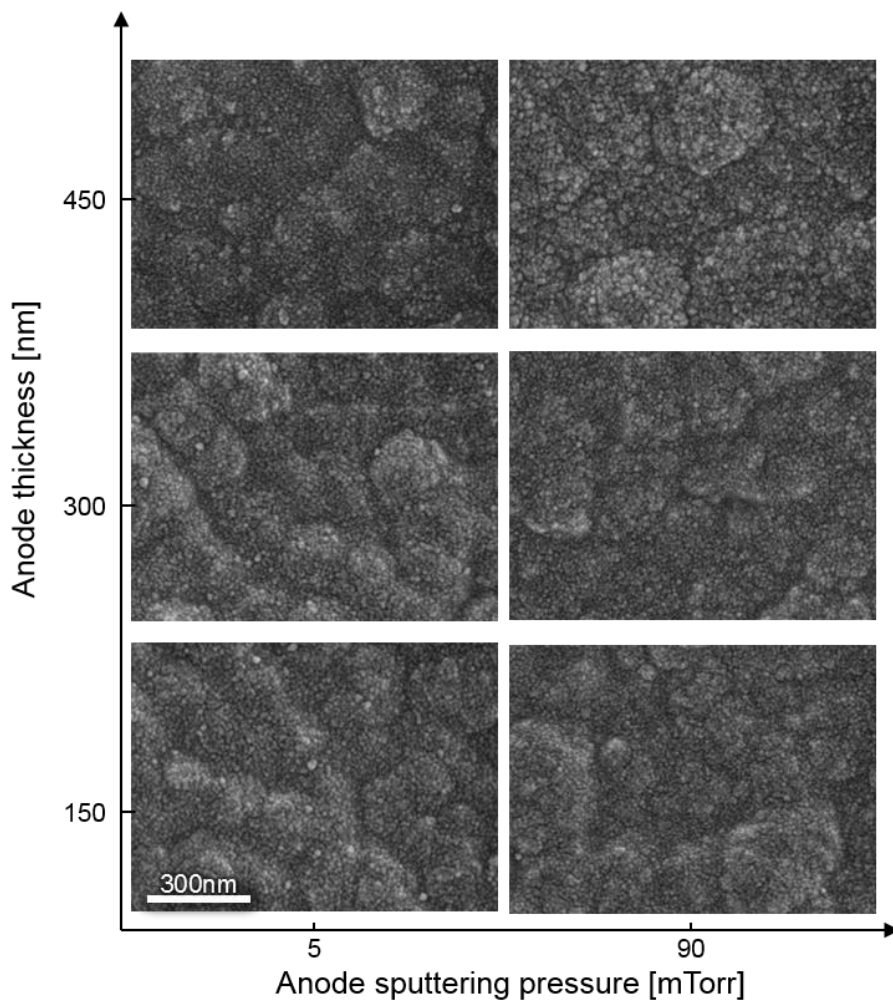


Figure 2.9 Surface morphologies of the electrolytes

In terms of the concentration overpotential, poor mass transports lead to significant losses of the fuel cell performance. The mass transport in porous media is closely related to its pore distribution properties, so the electrode morphology can



substantially affect the concentration loss. In Figure 2.8, compared to the platinum films sputtered at 90 mTorr, the dense films deposited at 5 mTorr showed that the surface morphology consisted of larger clusters and less pores. As the films became thicker, the number and the size of the pores on the dense platinum film surfaces greatly decreased. On the surface of 450 nm thick dense platinum anode, the pores were hardly observed and their sizes were far smaller than those on less thick dense films. This fully dense morphology of the cell might have hindered the gas supply to the interface between the anode and the electrolyte, causing the reactant depletion at reactive sites and the severe voltage drop at high current densities, as shown in Figure 2.2.

Electrochemical reactions in fuel cells are known to take place at the triple phase boundary (TPB), therefore the activation overpotential which governs the fuel cell performance in the low current region is closely related to the TPB density at the electrode/electrolyte interface. As previously indicated in Figure 2.9 and Figure 2.10, the morphologies of the electrolyte/cathode interface and the cathode surface were adjusted to be similar. Consequently, the TPB densities at the cathode sides for the oxygen reduction reactions (ORRs) do not seem to be the fundamental reason for different cell reactivities. By contrast, in Figure 2.8, the TPB density at the

anode/electrolyte interface seems to differ according to the porosity and the thickness of the anode. The anodes sputtered at 90 mTorr seemed to have higher TPB densities than those sputtered at 5 mTorr. This could facilitate the hydrogen oxidation reactions (HORs) at the anode side, contributing to lower activation overpotentials of the porous anode cells as shown in Figure 2.2. Moreover, in the surface image of the platinum film sputtered at 90 mTorr with thickness of 150 nm, the porous platinum was only deposited on the rib of the AAO, leaving the AAO pores not to be fully covered. The thicker the porous platinum became, the more the AAO pores were clogged by the porous catalyst layer increasing the TPBs. The increased TPB density at the anode side was attributed to the performance enhancement shown in Figure 2.2 (b) by promoting the HORs.

Consequently, in the architecture of the thin-film SOFC based on the AAO, a more porous structure of the platinum anode can provide more efficient reactant deliveries and higher TPB densities that reduce the activation and the concentration losses. The cell performance can be furthermore enhanced by optimizing the porous anode structure in consideration of the AAO pore size and distribution.

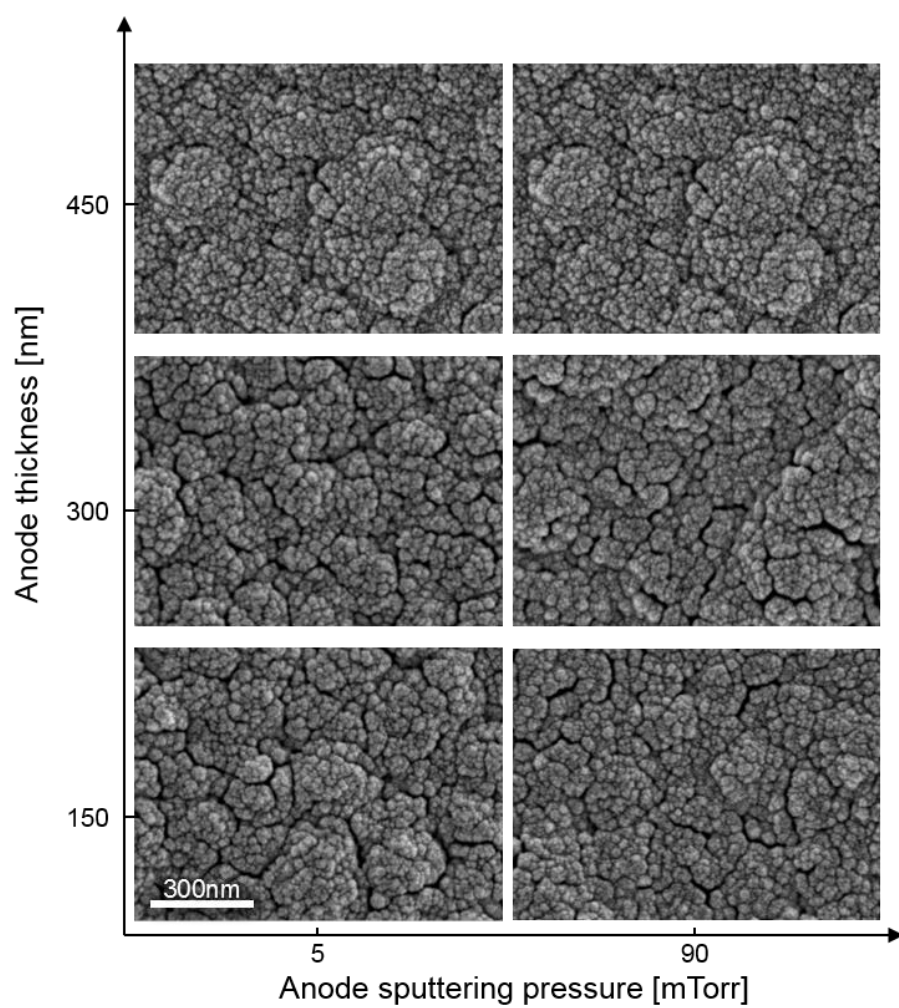


Figure 2.10 Surface morphologies of the cathodes

## 2.6 Conclusion

The AAO based thin-film SOFCs by applying various structures of anodes were successfully fabricated. All components including the anode, the electrolyte and the cathode were achieved by sputtering. In other words, the entire fabrication of the cells was carried out in the same chamber. This simple process can enhance the cost and time efficiency of the cell fabrication, while it moderates possible contaminations of the samples. It was demonstrated that the fully dense and defect-free YSZ electrolyte with thickness of hundreds of nanometers could be obtained by the sputtering process even on the various anode structures. Moreover, the porous platinum anode structure on the AAO template can improve the fuel cell performance by enhancing the TPB density and the fuel gas transport. Therefore, extensive researches on the optimization of the anode structure and the anode/electrolyte interface are furthermore required to improve the performance of the thin-film SOFC with the cell architecture based on the AAO substrates.

# CHAPTER 3      ATOMIC LAYER DEPOSITION OF YTTRIA STABILIZED ZIRCONIA FOR ENHANCED REACTIVITY AND STABILITY OF SOLID OXIDE FUEL CELLS

## 3.1 Introduction

Recently, the fabrication of thin-film SOFCs is in progress in order to lower ohmic losses below 500 °C, which are composed of only few tens or hundreds nanometer thick electrolyte [27], [39], [41], [61]–[64]. In the process of the fabrication of nano-sized thin-film SOFCs, the thermomechanical issues should inevitably be taken into account [17], [46], [54], [64]. In consideration of these difficulties, nano-porous templates were suggested as substrates to support thin-film fuel cells for higher mechanical stability and efficient gas delivery [34], [44], [48].

It has been demonstrated that where thin films were supported by nano-porous AAO templates, their electrical and microstructural degradation could be significantly mitigated even at elevated temperatures [54]. In most of the early researches about thin-film fuel cells with porous substrates, low open circuit voltages (OCVs) were reported to be obtained due to the difficulty of depositing a gas-tight electrolyte with

the thickness of submicrometer on the porous substrates [43], [44]. However, as the fabrication of thin-film SOFCs using various deposition techniques has been developed, extremely thin electrolytes on the porous substrates were successfully demonstrated without any gas leakage [25], [26], [46]–[48], [63], [65], [66]. It has been reported that successful fabrication of the intermediate temperature SOFCs with only 100 nm thick YSZ which was obtained by spin-coating the chemical solution on the porous anode support [25]. However, compared to the wet-chemical deposition techniques, in vacuum-assisted thin-film techniques, the atmosphere of the deposition can be controlled more carefully and strictly because the entire process takes place in the vacuum chamber [17], [67]. Thus, vacuum-assisted deposition methods such as sputtering, pulsed laser deposition (PLD) and atomic layer deposition (ALD) are more widely used for the fabrication of thin-film SOFCs [18], [29], [45], [68]–[70]. Unlike PLD process, which is known to be difficult to scale-up the process, sputtering and ALD methods, might be applicable to industrial production because they are able to promote mass production and uniform deposition over large scale of area. Moreover, ALD, a modified CVD technique, can achieve isotropic deposition with conformal covering over three-dimensional substrates without

pin-holes by building one mono-atomic layer after another [39]. Therefore, ALD has been reported as a key technique to obtain comparable OCVs in the fabrication of the thin-film SOFCs supported by nano-porous substrate [46]–[48], [56].

For nano-crystalline thin films, their microstructure and electrical conduction properties, which can directly affect the fuel cell performance, may vary with different deposition techniques [17], [67]. Moreover, for thin-film SOFCs with free standing structures, it has been reported that YSZ electrolytes produced by ALD represented superior electrochemical performance than YSZ electrolytes deposited by sputtering [58], [71]. However, for thin-film SOFC supported by nano-porous substrates, the effects of the deposition technique on the electrochemical performance of SOFCs have not yet been explored, even though it is reported that ALD layers can solve the pin-hole problems.

In this study, thin-film SOFCs supported by AAO substrate were fabricated with YSZ electrolytes deposited by different thin film techniques, and examined their differences in terms of electrochemical reactivity with the reasons expected to cause the differences. Furthermore, the effects of deposition techniques for YSZ electrolytes on long term stability of thin-film SOFCs on nano-porous AAO were demonstrated.

## 3.2 Experimental Details

### 3.2.1 Thin–Film Deposition

In this study, YSZ films were produced by two different thin film deposition processes: sputtering and ALD. First, the YSZ films via sputtering were produced by using an  $\text{Y}_{16}\text{Zr}_{84}$  alloy target at 200 W of RF (radio frequency) power. The atmosphere of the sputtering chamber was 5 mTorr of mixed gas which consisted of 80 % of argon and 20 % of oxygen. The substrate was not heated during sputtering, thus the YSZ thin film was deposited at room temperature. ALD YSZ thin films were fabricated by the sequential deposition of zirconia and yttria by using a custom–made ALD system. Commercial tetrakis (dimethylamido) zirconium ( $\text{Zr}(\text{NMe}_2)_4$ ) and tris (methylcyclopentadienyl) yttrium ( $\text{Y}(\text{MeCp})_3$ ) were used as precursors for zirconia and yttria, respectively. The zirconium and yttrium precursors were respectively heated to 70 °C and 140 °C, while the substrate in the ALD chamber was heated to 250 °C. Both oxides were produced by the sequential deposition of pulsing each precursor, purging ligands and residual reactants, pulsing oxygen as oxidant, and purging byproducts [39], [48], [56]. An YSZ deposition cycle consisted of



consecutive four zirconia deposition sequences and one yttria sequence. The deposition rate of the ALD YSZ thin film was about 1 Å/cycle.

### 3.2.2 Cell Fabrication

For fuel cell test, commercial AAO (Synkera Technology Inc.) with lateral dimension of  $1\text{ cm} \times 1\text{ cm}$ , a thickness of  $100\text{ }\mu\text{m}$ , and a pore diameter of  $80\text{ nm}$  were used as substrates to support the thin-film SOFCs. A dense Pt anode with a thickness of  $300\text{ nm}$  was deposited on the entire surface of the AAO substrate by direct current (DC) sputtering at  $200\text{ W}$  at room temperature with an Ar pressure of  $5\text{ mTorr}$ . YSZ electrolytes were deposited on the anode layer with a total thickness of  $500 \sim 550\text{ nm}$  by different thin film techniques. A porous Pt cathode with a thickness of  $150\text{ nm}$  was deposited by DC sputtering at  $100\text{ W}$  at room temperature with an Ar pressure of  $90\text{ mTorr}$ . A shadow mask was used to produce the active area of  $1\text{ mm} \times 1\text{ mm}$ , as mentioned in CHAPTER 2.

The anode side of the fuel cell sample was sealed on a custom-made metal chamber where dry hydrogen of  $20\text{ sccm}$  was fed as the fuel. The patterned cathode electrode was exposed to oxygen in ambient air. Polarization and impedance characteristics were measured by a commercial electrochemical impedance spectroscopy (Solatron Analytical, 1260/1287) at  $450\text{ }^{\circ}\text{C}$  with  $V_{\text{AC}} = 30\text{ mV}$  and  $V_{\text{DC}} = 0.5\text{ V}$ .

### 3.2.3 Characterization

The focused ion beam (FIB) and scanning electron microscope (SEM) were used to investigate the cross-sectional images of fabricated cells. Surface topography and roughness of the electrolyte layer were investigated under tapping mode of atomic force microscopy (AFM). Chemical composition and crystallinity of the YSZ thin films were analyzed by X-ray photoelectron spectroscopy (XPS) and X-ray diffraction (XRD), respectively. Change in morphology of porous Pt cathode arising from operating at 450 °C was examined by field emission secondary electron microscope (FE-SEM).

### 3.3 Results and Discussion

#### 3.3.1 Configurations of Fabricated Cells

To examine the reactivity and the stability for nano-porous substrate supported thin-film SOFCs with YSZ electrolytes produced by sputtering and ALD process, three cells of different electrolyte were employed to each cell: YSZ electrolyte deposited by sputtering, YSZ layer by ALD, and multilayered YSZ composed of ALD layer on the sputtered layer. For all cells, the anode and the cathode layers were deposited under the same conditions, which were described in previous section. Figure 3.1 shows the cross-sectional images of the fabricated cells. In each cell, the thicknesses of the electrolyte, the anode and the cathode were respectively 500~550 nm, 300 nm, and 150 nm.

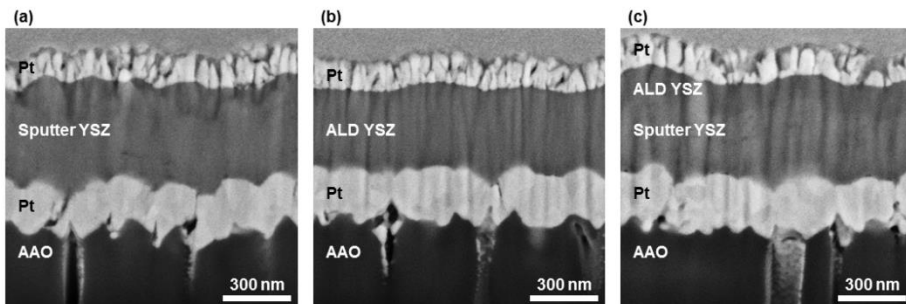


Figure 3.1 Cross-sectional images of the fabricated cells

First, the YSZ electrolyte of the first cell was deposited by sputtering, and that of the second cell was produced by ALD to compare the fuel cell characteristics of the same electrolyte materials made by different deposition techniques in terms of reactivity and stability. Lastly, a multilayered YSZ electrolyte, which is composed of the ALD YSZ layer on top of the sputtered YSZ layer, was employed to the third cell. The last cell was fabricated to confirm that the differences in electrochemical performance between the first cell (the sputtered YSZ cell) and the second cell (the ALD YSZ cell) originated from the difference in the reactivity of the cathode side.

### 3.3.2 Electrochemical Reactivity of the Fuel Cells

The three fabricated cells were electrochemically characterized at 450 °C to investigate the effects of the electrolyte deposition technique on the fuel cell performance. Figure 3.2 depicts the current density–voltage curves of the three cells. The open circuit voltage (OCV) values of all cells were measured to be about 1~1.1 V, which are close to the theoretical values calculated by the Nernst equation. It means that the YSZ electrolytes of the three cells were well-produced and dense enough to avoid the gas leakage and the electrical shortage, although they are known as inherent problems in the thin film fuel cells supported by the porous substrates [46].

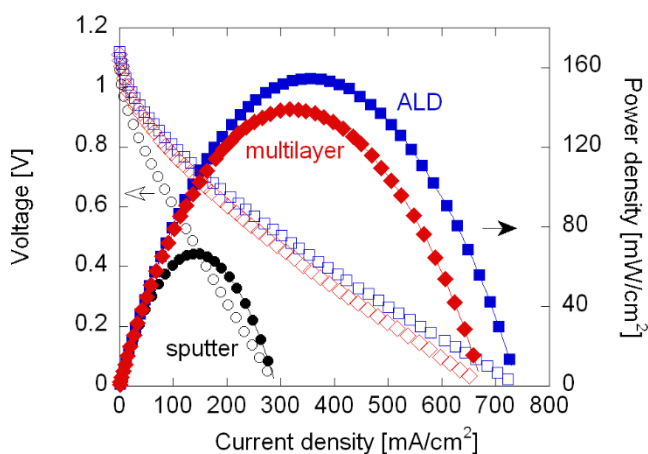


Figure 3.2 Current density–voltage curves of the fabricated cells

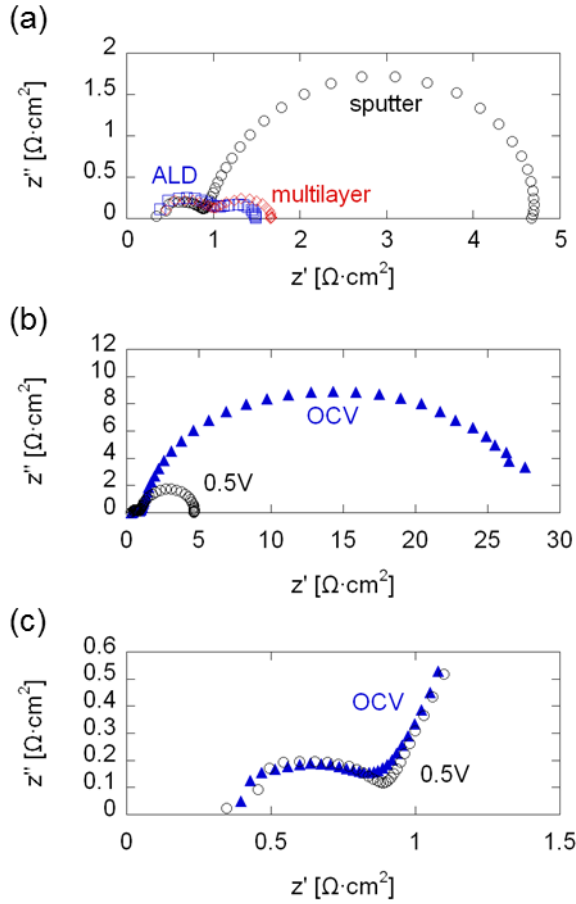


Figure 3.3 Electrochemical impedance spectra of (a) the fabricated cells at 0.5 V and (b) the sputtered YSZ cell at OCV and 0.5 V, and (c) the plots magnified at high-frequencies

The peak power densities of the sputtered YSZ cell, the ALD YSZ cell and the multilayered YSZ cell were 66.2, 154.6 and 139.1  $\text{mW}/\text{cm}^2$ , respectively. The electrochemical performance of the sputtered YSZ cell was much lower than that of the ALD YSZ cell. It indicates that the electrochemical properties of the

YSZ electrolyte produced by the ALD process were much better than that of the sputtered YSZ membrane. Moreover, the current density–voltage curve of the multilayered YSZ cell shows similar fuel cell performance to that of the ALD YSZ cell. Thus, it can be concluded that modifying the cathode side interface by the ALD process significantly improves the electrochemical performance in the AAO based thin–film SOFCs.

The electrochemical impedance spectroscopy analysis was conducted to assess the reason for the difference in the performance as shown in Figure 3.2. Figure 3.3 (a) represents Nyquist plots for three cells measured at 0.5 V. The high–frequency intercepts and the magnitude of the high–frequency semicircles were quite similar in all the cells, while the low–frequency semicircle of the sputtered YSZ cell was markedly bigger than the others. It means that the low–frequency responses caused the difference in electrochemical performance as shown in Figure 3.2. In general, low–frequency semicircles in Nyquist plots are closely related to the electrochemical kinetics in electrodes, while high–frequency semicircles are related to the electrolyte processes [58]. Figure 3.3 (b) shows the electrochemical impedance spectra for the sputtered YSZ cell measured at OCV and 0.5 V. The high–frequency semicircle was independent on the variation of the



voltage, while the magnitude of the low-frequency semicircle noticeably varied with the DC voltage, which indicates that the low frequency-responses were caused by electrode polarizations.

It has been reported that the oxygen reduction reactions (ORR) are much more sluggish than the hydrogen oxidation reactions (HOR) [13]. Therefore, the electrode polarization impedance, that is the magnitude of the high-frequency semicircle in the Nyquist plots, is dominated by the electrochemical reactivity at the electrolyte/cathode interface. Consequently, the most major reason of the lower electrode resistance in the ALD YSZ cell would be the enhanced cathodic reactivity at the interface between ALD YSZ and Pt. Furthermore, the electrochemical impedance spectra of the multilayered YSZ cell in Figure 3.3 also supports that designing the reactive interface at the cathode side is crucial for the fuel cell performance. The low-frequency semicircle of the multilayered YSZ cell was quite similar to that of the ALD YSZ cell. It indicates that the only 100 nm of the ALD YSZ layer added between the sputtered YSZ electrolyte and the Pt cathode could significantly enhance the fuel cell performance. Therefore, in thin film SOFCs, the ALD YSZ layer facilitates the cathodic reactions, consequently improving the fuel cell performance.

Figure 3.4 shows the topography of the electrolyte surfaces of

the fabricated cells. The root-mean-square (RMS) values of the surface roughness for the sputtered YSZ, the ALD YSZ and the multilayered YSZ were 26 nm, 13 nm and 17 nm, respectively. In addition, the ratios of the surface area to projected area were 1.19, 1.02 and 1.07, respectively. It has been reported that the surface of the YSZ sputtered on Si wafer was rougher than that of the ALD YDZ films deposited on the Si substrate [67]. Thus, the results of the AFM analysis are quite reasonable.

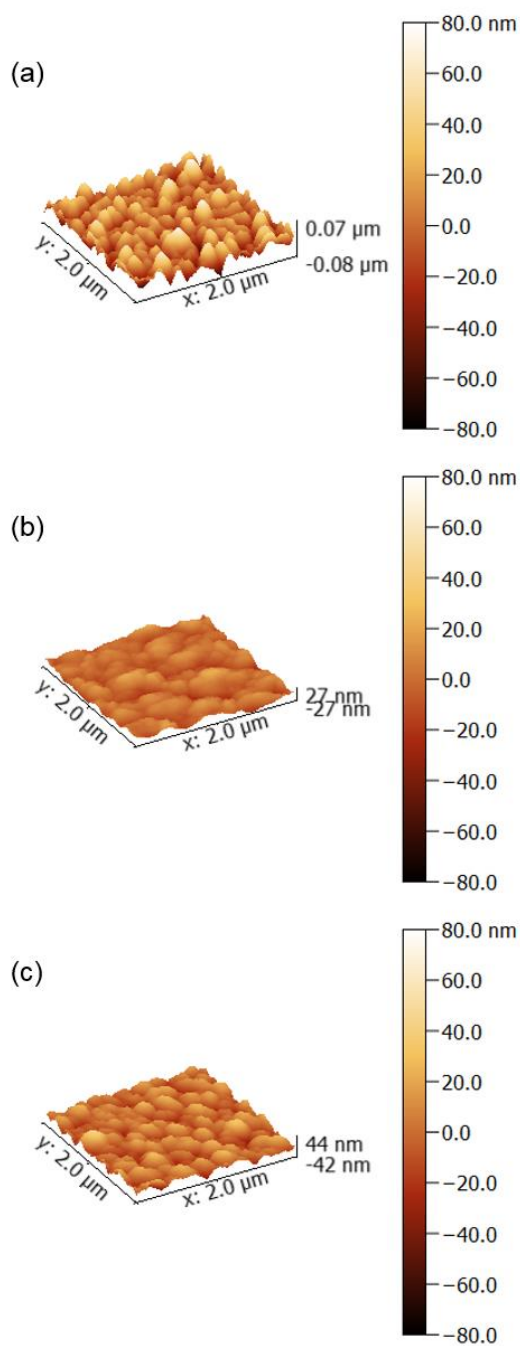


Figure 3.4 Topography of the electrolyte surfaces of (a) the sputtered YSZ cell, (b) the ALD YSZ cell and (c) the

multilayered YSZ cell

It is known that the electrochemical reactivity is improved by increasing the number of reaction sites per unit area [13]. Thus, a highly rough electrolyte surface is more favorable for electrochemical reactions than a smooth surface.

Table 3.1 Surface properties calculated from the AFM measurements

	Sputtered YSZ	ALD YSZ	Multilayered YSZ
Scan area [ $\mu\text{m}^2$ ]	4	4	4
RMS [nm]	21.1	6.98	10.85
Surface area [ $\mu\text{m}^2$ ]	4.77	4.07	4.24

However, although the electrolyte surface of the sputtered YSZ cell was rougher than those of the ALD YSZ cell and the multilayered YSZ cell, later two cells showed much higher reactivity than the sputtered YSZ cell as shown in Figure 3.2, and Figure 3.3. Based on these results, it can be concluded that another contributing factor, besides the surface roughness, was responsible for the difference in the cathode reactivity among the fabricated cells. As a result, besides the roughness of the YSZ electrolytes, there was another factor to contribute to the

difference in the fuel cell performance.

In general, the concentration of yttria in YSZ determines oxygen vacancies and charge compensation effects [13]. Thus, the strength of the yttria doping affects the ionic conductivity. To examine the yttria concentration in the YSZ films, XPS analysis was conducted for the sputtered YSZ and the ALD YSZ on Si wafer. As shown in Table 3.2, the yttria concentration in the sputtered YSZ film was 8.6 mol %, whereas it was 10.0 mol % in the ALD YSZ film. While an YSZ film with the yttria doping ratio of 8 mol % is known to show optimal ion conductivity, Chao *et al.* have reported that the oxygen incorporation at the platinum–YSZ interface was enhanced at higher yttria concentration than 8 mol % [72], [73].

Table 3.2 XRD results of YSZ thin films

composition		Sputtered YSZ		ALD YSZ	
		as deposited	annealed	as deposited	annealed
atomic conc. [%]	Y 3d	5.09	4.92	5.74	6.03
	Zr 3d	27.03	26.45	25.76	25.39
	O 1s	67.88	68.63	68.50	68.58
yttria doping		8.60	8.51	10.02	10.62

Thus, one can expect that the ALD YSZ electrolyte may show better oxygen incorporation because of its higher vacancy density near the cathode–electrolyte interface. However, the difference in the yttria concentration of the both films does not seem to be significant enough to enhance the peak power density of the ALD YSZ cell more than twice as the peak power density of the sputtered YSZ cell [72]. Moreover, as shown in Figure 3.3, the similarity of high–frequency semicircles of the sputtered YSZ cell and the ALD YSZ cell implies that the effects of the chemical compositions on the oxygen ion conductivity through the electrolytes were negligible in this case.

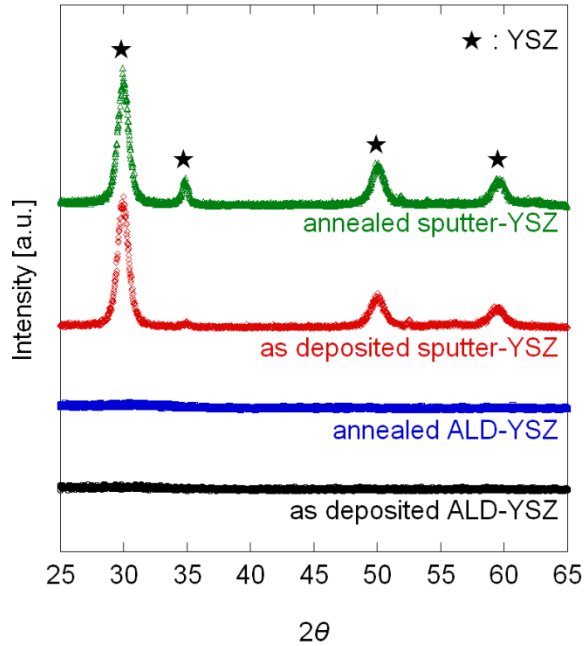


Figure 3.5 XRD patterns of the sputtered YSZ and ALD YSZ before and after annealing

Figure 3.5 shows XRD patterns for the sputtered YSZ and ALD YSZ thin films. It represents that the microstructure of the ALD film was amorphous, while the sputtered YSZ film was polycrystalline. Shim *et al.* has demonstrated superior electrochemical properties of ALD YSZ films with amorphous structure and nano-granular morphology [58]. It was reported that the electrochemical performance of the thin-film fuel cell employing the ALD YSZ thin film as an electrolyte was higher than the cell employing the RF-sputtered YSZ membrane. In addition, it has been reported that the grain boundary is more

reactive for oxygen exchanges and incorporation than the bulk grain [58], [71]. Thus, the high grain boundary density and the amorphous crystallinity of the ALD YSZ thin film may improve the oxygen reduction reactivity at the interface between YSZ electrolyte and Pt cathode. Moreover, it can be also supported by the  $j$ - $V$  and the electrochemical impedance characteristics of the multilayered YSZ cell. As shown in Figure 3.2 and Figure 3.3, they was fairly close to those of the ALD YSZ cell rather than those of the sputtered YSZ cell. Therefore, the enhanced cathode reactivity by the addition of the ALD YSZ layer on the cathode side mostly originated in its microstructural superiority compared to the sputtered YSZ layer.



### 3.3.3 Enhanced Long-Term Stability of the ALD-YSZ

To examine the long-term stability of the cells with the electrolytes deposited by different thin-film techniques, galvanostatic measurements were conducted at constant current density of  $100 \text{ mA/cm}^2$  for the sputtered YSZ cell and the ALD YSZ cell. Figure 3.6 shows the results of the galvanostatic measurements of the sputtered YSZ cell and the ALD YSZ cell. The measurements were performed at  $450^\circ\text{C}$  for about 45 min. The voltage of the sputtered YSZ cell drastically dropped to 0 V at  $100 \text{ mA/cm}^2$  in 45 min, while the voltage of the ALD YSZ cell decreased by only 3.71 % (from 0.727 V to 0.700 V).

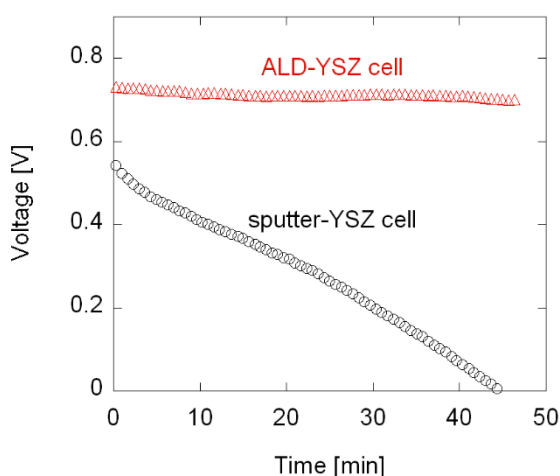


Figure 3.6 Galvanostatic measurements of the sputtered YSZ cell and the ALD YSZ cell

Figure 3.7 shows the current density–voltage curves of the sputtered YSZ cell measured before and after the galvanostatic test. The maximum power density of the sputtered YSZ cell was reduced from 66.2 mW/cm<sup>2</sup> to 17.6 mW/cm<sup>2</sup> in 45 min, while that of the other cell hardly decreased from the initial performance. Figure 3.8 shows the electrochemical impedance spectra, which were measured before and after the galvanostatic measurement for the sputtered YSZ cell. The low–frequency semicircle increased remarkably after the aging test, whereas the ohmic resistance and the high–frequency semicircle hardly changed. It indicates that the fuel cell performance degradation shown in Figure 3.7 was mainly caused by the increase of the cathodic impedance.

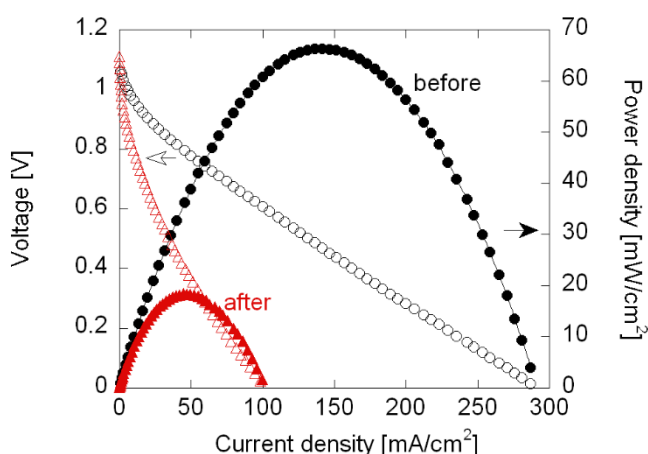


Figure 3.7 Current density–voltage curves of the sputtered YSZ cell before and after the galvanostatic measurement.

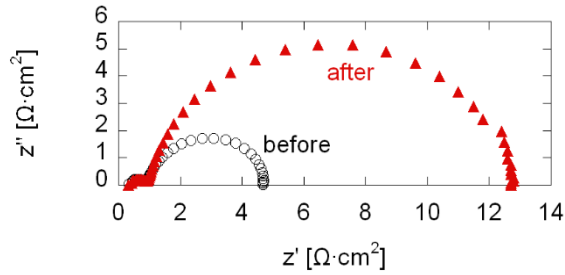


Figure 3.8 Electrochemical impedance spectra of the sputtered YSZ cell before and after the galvanostatic measurement

It is known that the electrochemical reactions take place at the triple phase boundaries where electrolyte, gas, and electrode are in contact [13], [14]. Thus, it can be assumed that the degradation of the cathodic reactivity of the sputtered YSZ cell originates from any changes in the triple phase boundaries at the interface of the YSZ electrolyte and the Pt cathode.

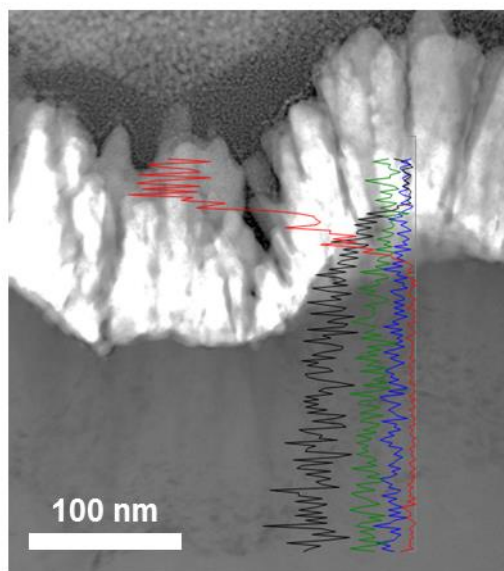
First, to investigate compositional and microstructural change in the electrolyte, the sputtered YSZ film and the ALD YSZ film were annealed for 10 hours at 450 °C. As shown in Table 3.2, the changes in the results of the XPS measurements for both sputtered film and ALD film became negligible after the annealing. From the XRD results depicted in Figure 3.5, the patterns became more distinct in both samples after the annealing process, but there were yet some substantial

differences in terms of crystallinity. Hence, the minor changes in the microstructures could be partially responsible for the low stability of the sputtered YSZ cell, but they do not seem to be dominant.

Figure 3.9 shows the scanning transmission microscope image and the energy dispersive spectroscopy (EDS) profile of the cathode and the electrolyte of the sputtered YSZ cell. As shown in Figure 3.9, the intermixing of YSZ and Pt at their interface during the fuel cell test was not observed. Therefore, the minor changes in the YSZ electrolytes may not have been the main reason to cause the great difference in the degradation tendencies of the electrode processes in the sputtered YSZ cell and the ALD YSZ cell.

Other possible mechanisms can include any changes in Pt morphology or temperature driven agglomeration of Pt layer. Pt has been known as one of the most commonly utilized electrode materials due to its catalytic effect and low electrical resistance [54]. It is known that Pt thin film electrode agglomerates to form larger clusters at fuel cell operation temperature due to the inherent thermodynamic instability of metal thin films on oxidic substrates [74]. The agglomeration of Pt electrode decreases the TPB length at Pt/YSZ interface, subsequently leading to the degradation of the fuel cell performance [75].

(a)



(b)

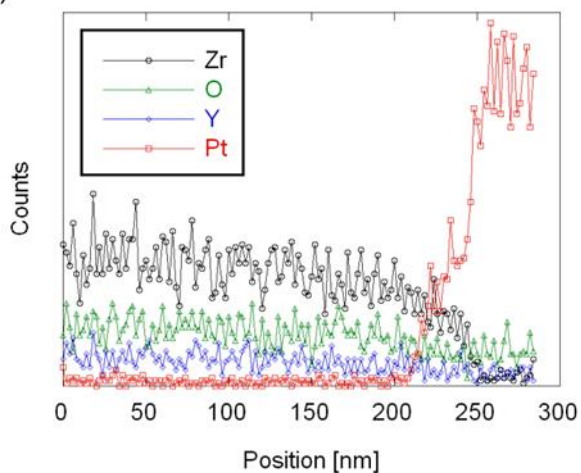


Figure 3.9 A STEM image and an EDS profile of the cathode and the electrolyte of the sputtered YSZ cell.

Figure 3.10 and Figure 3.11 respectively show the secondary electron microscope images of Pt morphologies on the

sputtered YSZ and the ALD YSZ films before and after annealing for 10 h at 450 °C. Before the annealing, Pt on the sputtered YSZ film formed larger clusters and showed higher surface roughness than the one on the ALD YSZ film. However, the morphology of the sputtered YSZ surface was hardly changed after the annealing as shown in Figure 3.12.

Figure 3.13 shows the topographies of the Pt cathodes of the sputtered YSZ cell and the ALD YSZ cell. The roughness RMS values of the sputtered YSZ cell and the ALD YSZ cell were 27.0 and 12.8 nm, respectively.

The relatively uneven surface of the Pt on the sputtered YSZ film can be entirely ascribed to the rougher topography of the sputtered YSZ shown in Figure 3.4, because the Pt sputtering condition was identical for both samples. In spite of the different surface topography of the two samples, the variation of the porosity was not substantial.

On the other hand, the porous Pt cathode on the sputtered YSZ film agglomerated more severely than the porous Pt cathode on the ALD film after annealing, as shown in Figure 3.10 (b) and Figure 3.11 (b). Thus, it can be speculated that the reduction of the TPB length at the cathode side of the sputtered YSZ cell was far more severe than that of the ALD YSZ cell. More drastic reduction of the TPB length resulted in the performance

degradation of the sputtered YSZ cell as shown in Figure 3.7.

When thin films are annealed, atoms will diffuse to reduce the local excess chemical potentials by increasing the radius of curvature at the points, and then, dewetting will proceed at substrate–ambient interfaces, as described by Jiran and Thompson [76]–[78]. The rougher surface of the sputtered YSZ, which indicates smaller radius of curvature, might cause more drastic aggregation of Pt on the surface. Forming larger clusters of Pt on the YSZ reduces the length of the triple phase boundaries, consequentially, reducing the cathode reactivity.

Hence, highly smooth and uniform thin film YSZ fabricated by ALD process is more desirable for the stability of Pt cathode than YSZ film deposited by sputtering process. Consequently, applying ALD process on the fabrication of the electrolyte for the thin film SOFCs can substantially improve the durability as well as the performance.

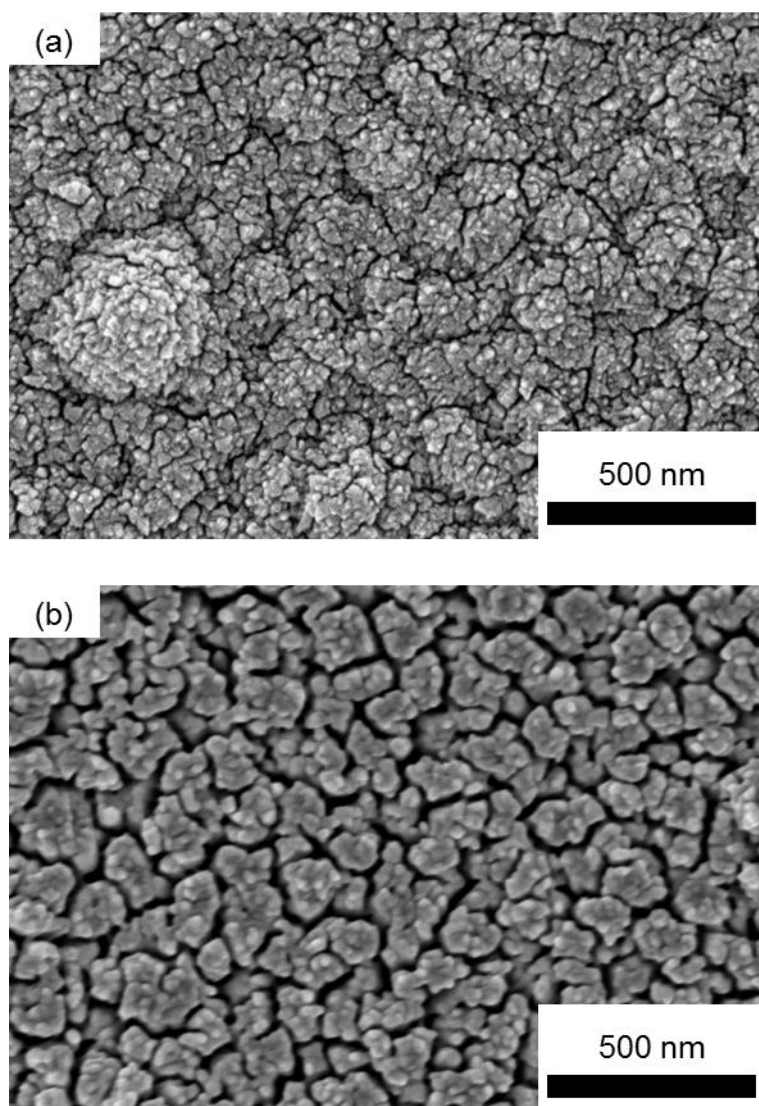


Figure 3.10 Morphologies of porous Pt cathode deposited on the sputtered YSZ thin film (a) before and (b) after annealing for 10 hours at 450 ° C



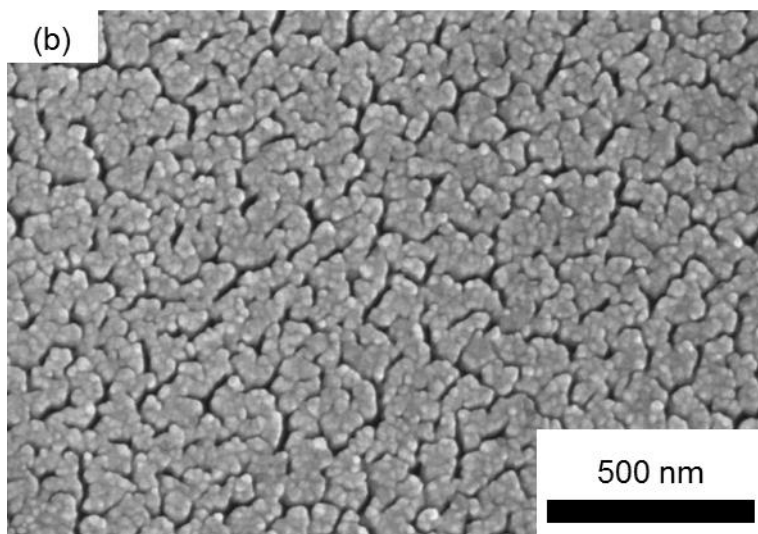
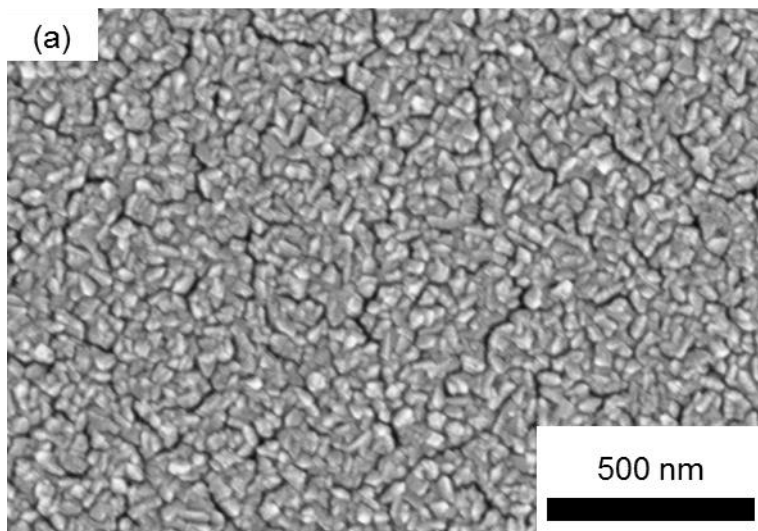


Figure 3.11 Morphologies of porous Pt cathode deposited on the ALD YSZ thin film (a) before and (b) after annealing for 10 hours at 450 ° C

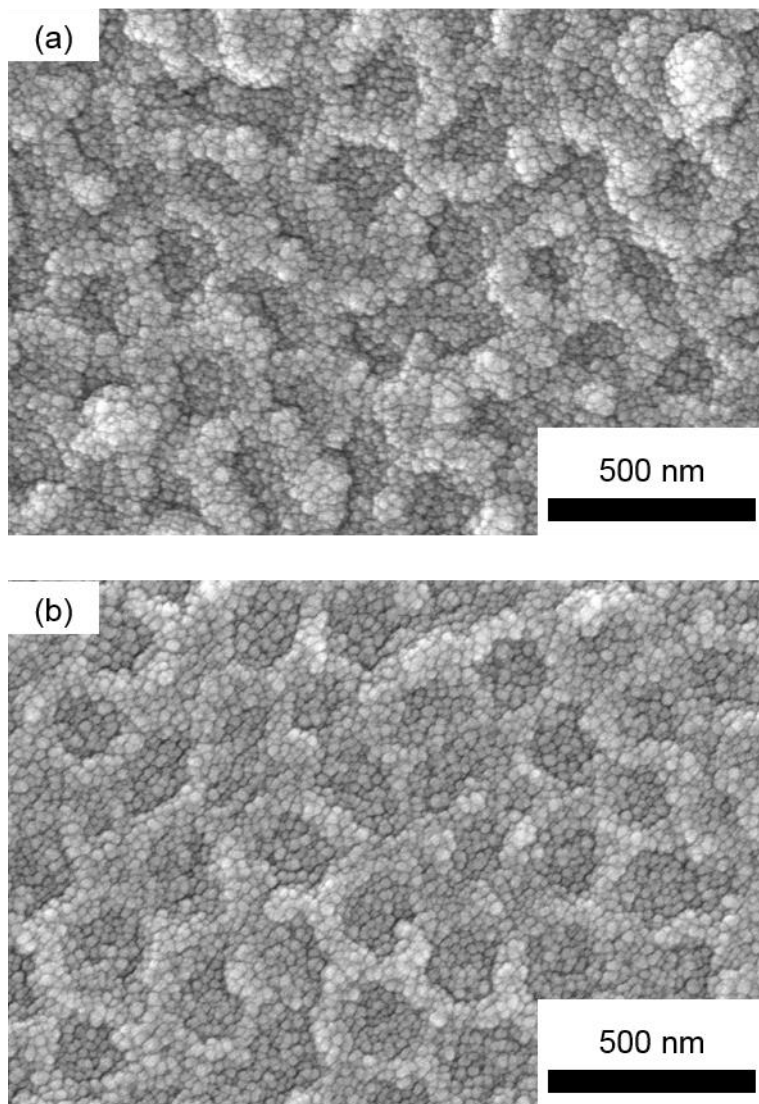


Figure 3.12 Morphologies of the sputtered YSZ thin film (a) before and (b) after annealing for 10 hours at 450 ° C

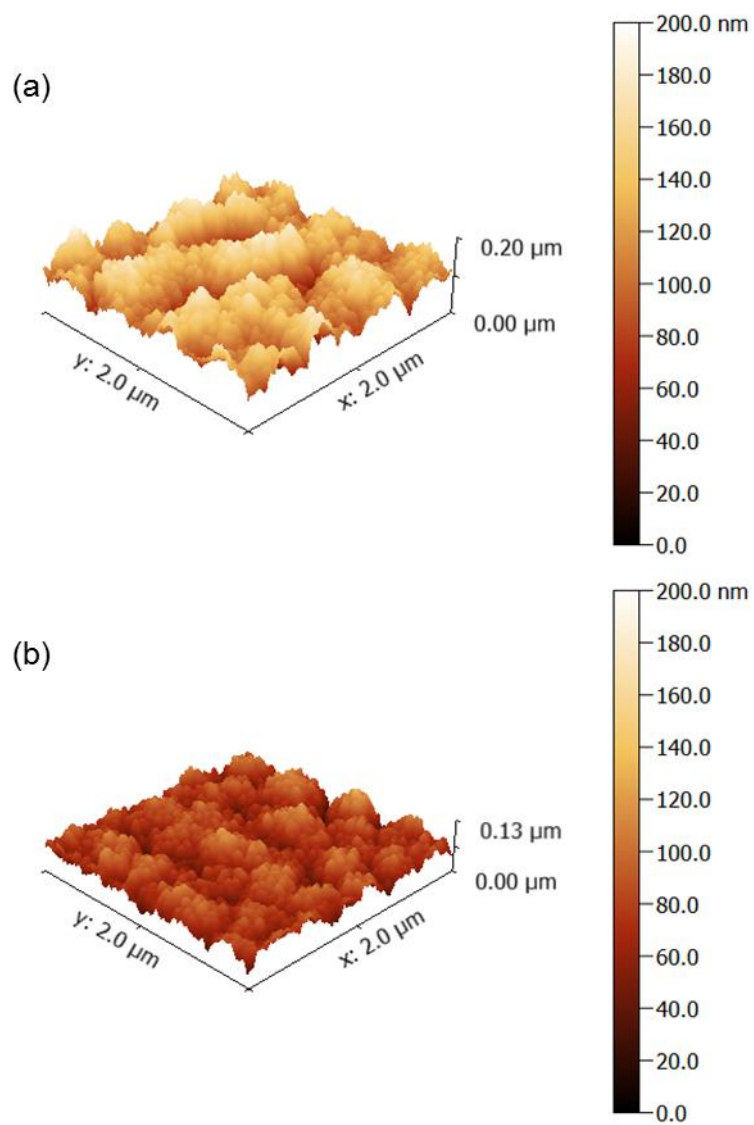


Figure 3.13 Topographies of the Pt cathodes on (a) the sputtered YSZ and (b) the ALD YSZ films

### 3.4 Conclusion

In this study, it was demonstrated that the electrochemical reactivity and the thermal stability of the thin-film SOFCs can be significantly improved by deposition of the electrolyte films via the ALD process on nano-porous substrates. The amorphous and nano-granular structures of the ALD films enhanced the cathodic reactivity and the electrochemical performance of fabricated cells. Retarded agglomeration of the Pt layer due to the smooth and uniform surface of ALD films enhanced the thermal stability at elevated temperatures. The observed higher reactivity and stability of the ALD cells substantiate that ALD process can play a crucial role in developing the thin film SOFCs using nano-porous substrates by improving the cell performance and the thermos-mechanical stability as well as clogging pinholes in the electrolyte.

## CHAPTER 4      SCALE UP OF THIN–FILM SOLID OXIDE FUEL CELLS ON NANO–POROUS SUBSTRATES

### 4.1 Introduction

Although the thin–film SOFCs employing the free standing architecture showed high area normalized power density at low temperatures ( $<500\text{ }^{\circ}\text{C}$ ), the most free–standing fuel cells have been demonstrated in dimension of only tens or hundreds of micrometers. To utilize as power sources of electric devices, it is necessary to scale the total power output of the thin–film fuel cells up.

Recently, Tsuchiya *et al.* succeeded to extend the free–standing thin–film SOFCs in millimeter–scale in lateral dimensions by adding platinum grid [50]. Before their research, the lateral size of the free–standing thin–film SOFCs had been limited to a few hundred micrometers [38], [39], [41], [62], [64], [79]–[81]. Therefore, the total power output had not been sufficient for practical applications despite their extremely high power densities. The active area of the cell from Tsuchiya’s research team was  $13.5\text{ mm}^2$  and the peak power density at  $510\text{ }^{\circ}\text{C}$  was reported as  $155\text{ mW/cm}^2$ ; eventually the

total power of the unit cell was about 21 mW. However, even though the metallic grid had successfully functioned as mechanical supports, a few cases of buckling were reportedly observed in the free-standing membranes with the thickness of only tens of nanometer. On the other hand, in the porous substrate supported thin-film SOFCs, the thickness of the substrates is tens or hundreds micrometers, which provides more mechanical stability. Owing to the enhanced mechanical stability, the porous substrate structures are more easily enlarged, leading to an increased level of total power.

In this study, thin-film SOFCs based on nano-porous substrate were successfully fabricated, and their active areas were as large as 25 mm<sup>2</sup>. For the electrolyte, we employed a submicron thick multilayered one to achieve a pinhole-free membrane. Also, we electrochemically characterized the fuel cells with different cathode morphologies, in order to figure out the effects of the cathode structure on ohmic and faradaic resistances of the fuel cells. Finally, we managed to develop an additional current-collecting structure on top of the cathode, which turned out to enhance the overall electrochemical performance of the fuel cells.

## 4.2 Experimental

### 4.2.1 Sample Preparation

A commercial AAO (Synkera Technology Inc.) template of 1 cm  $\times$  1 cm area and of 100  $\mu$ m thickness with 80 nm pores was used as substrate to support the thin-film SOFCs. A dense Pt anode composed of about 300 nm of thickness was deposited on the entire surface of the AAO substrate by direct current (DC) sputtering at 200 W at room temperature and 5 mTorr of Ar pressure. Subsequently, the multilayered electrolyte, composed of two ALD YSZ layers and a sputtered GDC layer, was deposited on the anode layer. The YSZ thin films were achieved by the co-deposition of zirconia and yttria by using a commercial ALD system (Plus-100, Quoros Co.). Both oxide materials were deposited by repeating the sequence of pulsing precursor, purging ligands and unreacted precursor, pulsing oxidant, and purging byproducts. Tetrakis (dimethylamido) zirconium,  $\text{Zr}(\text{NMe}_2)_4$ , and tris (methylcyclopentadienyl) yttrium,  $\text{Y}(\text{MeCp})_3$  were used as precursors of zirconium and yttrium, respectively. Ar gas (99.99 % purity) and  $\text{O}_2$  gas were respectively used as purging gas and oxidant gas. For more detailed description of the ALD YSZ by this system, please

refer to the related publications of our research team [48].

Table 4.1 Sputtering conditions of the electrodes and the current collector

		Background gas	Sputtering power [W]	pressure [mTorr]	Thickness [nm]
Anode	All cells	Ar	200	5	300
Cathode	Cell 1	Ar	100	90	200
	Cell 2, 3	Ar	100	30	200
Current collector	Cell 3	Ar	200	5	300

The GDC film was RF sputtered on the first ALD YSZ layer to be used as the primary electrolyte, owing to its high ionic conductivity at low temperatures. The sputtering conditions of the GDC layer were 50 W, at room temperature and mixed Ar/O<sub>2</sub> gas pressure of 5 mTorr. And then, the second ALD YSZ thin film was deposited on the GDC layer. The surface area of the electrolyte was adjusted to 8 mm × 8 mm through a mask. Furthermore, the Pt cathode layers were deposited by DC sputtering at different Ar pressures. The cathode of the first cell (cell 1) was DC sputtered at 90 mTorr of Ar pressure in order to make the electrode sufficiently porous, as demonstrated in many previous thin-film SOFCs researches. The cathode of the second cell (cell 2) was deposited at 30



mTorr of Ar pressure for denser morphology. The cathode layers of the both cells were sputtered at 100 W of sputtering power, at room temperature. Also, they were patterned through a shadow mask to have  $5\text{ mm} \times 5\text{ mm}$  of active areas. They were consistent in thickness of about 200 nm. Additionally, the third cell (cell 3) was fabricated by adding dense Pt current-collecting path on the cathode surface of the cell 2. The current-collecting path was DC sputtered through a physical mask with a single cross pattern, whose line width and thickness were 0.5 mm and 300 nm, respectively. The sputtering power and Ar pressure were set to 200 W and 5 mTorr. Figure 4.1 (a) schematically shows the structure of cell 1 and 2, while Figure 4.1 (b) represents the scheme of cell 3.

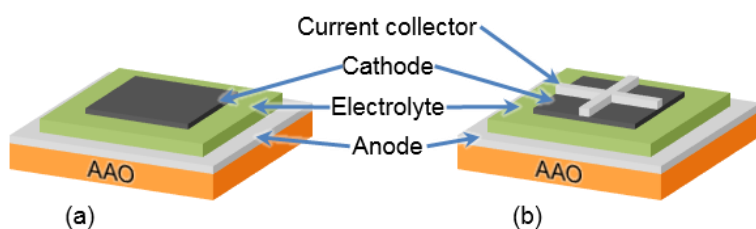


Figure 4.1 Schematics of (a) cell 1 and 2, and (b) cell 3

#### 4.2.2 Fuel Cell Test

The anode and the custom made metal ring were physically and electrically connected by using silver paste while the micro probe was used to collect the cathodic current. Ceramic adhesive (Aremco Products Inc.) was used to secure the gas tightness. The anode side was fed by dry hydrogen of 100 sccm as fuel while the cathode side was exposed to atmospheric environment for air-breathing. Polarization and alternating impedance (AC) characteristics were measured by a commercial electrochemical testing system (Solatron Analytical, 1260/1287). The 30mV AC amplitude and 0.5 V DC potential were applied during the electrochemical impedance spectroscopy (EIS) measurements. The fabricated cells were heated to 500 °C by halogen heaters in custom made furnace.

## 4.3 Results and Discussion

### 4.3.1 Morphologies of Fabricated Cells

Figure 4.2 shows the cross sectional image of cell 1. The multilayered electrolyte was formed in the thickness of about 750 nm. The cross sectional structure of cell 2 was almost identical to that of cell 1. However, as represented in Figure 4.3 (a) and (b), the cathode surface morphologies of the two cells were quite different. The cathode layer sputtered at higher Ar pressure was more porous than the one deposited at lower pressure. These results correspond with the previously reported researches on sputtered Pt thin films [82].

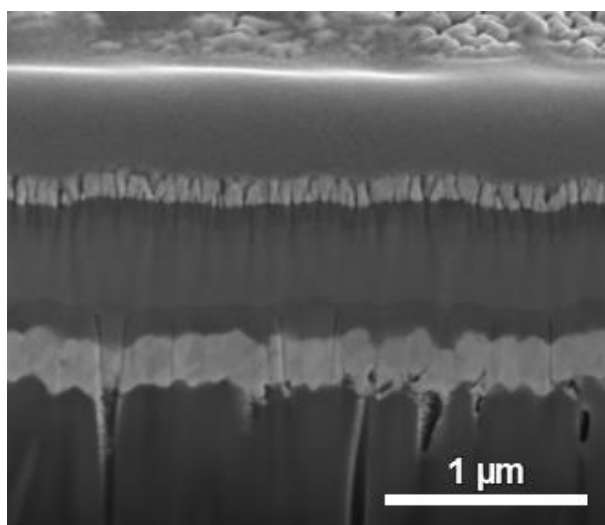


Figure 4.2 Cross-sectional imager of the fabricated cells

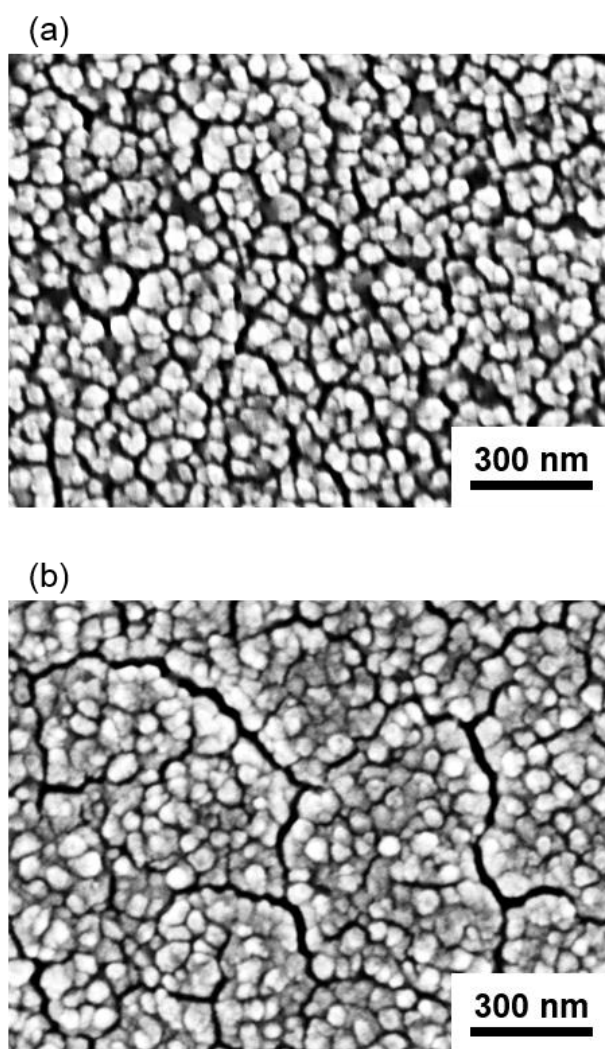


Figure 4.3 Morphologies of the Pt cathodes of (a) cell1 and (b) cell 2

#### 4.3.2 Effects of Cathode Porosity on Performance of Thin-Film Fuel Cells with Larger Active Areas

Figure 4.4 demonstrates the results of the electrochemical characterizations for cell 1 and 2 which were operated at 500 °C. As shown in Figure 4.4, the open circuit voltage (OCV) values of both cells were measured to be approximately 1~1.1 V. This indicates that the multilayered electrolyte (ALD YSZ-sputtered GDC-ALD YSZ) was dense enough to prevent the propagation caused by the porous substrate. Therefore, it can be concluded that the porous substrate supported thin-film SOFCs are highly reliable, when properly equipped with the ALD process. As shown in Figure 4.4, the peak power density of cell 1 and 2 were about 49.1 and 71.4 mW/cm<sup>2</sup>, respectively. The electrochemical impedance spectra of cell 1 and 2 in Figure 4.5 show more detailed information regarding the drop of the cell voltage. The solid lines were obtained by fitting with the equivalent circuit model. The faradaic resistance values of cell 1 and 2 were respectively evaluated as 1.14 and 1.29  $\Omega \cdot \text{cm}^2$  while the ohmic resistance values of cell 1 and 2 were evaluated as 2.42 and 1.5  $\Omega \cdot \text{cm}^2$ . Although the faradaic resistance of cell 1 was slightly lower than that of cell 2, the difference was not substantial in spite of the less porous

cathode of cell 2. On the other hand, the ohmic resistance value of cell 1 was evaluated  $1\ \Omega\cdot\text{cm}^2$  higher than the value of cell 2. Therefore, the ohmic resistance is regarded to be more responsible for different electrochemical polarizations of cell 1 and 2.

Ohmic overpotentials of the fuel cells are known to be governed by ionic conduction in electrolytes, which is far more sluggish than the electronic conduction in electrodes [13]. However, the ohmic resistances of cell 1 and 2 were considerably different even though both cells were equipped with identical electrolytes, with same structures and materials.

In general, resistance is proportional to the length of the conductor but inversely proportional to the conductivity and the cross sectional area of the conductor. The ionic conductivity of GDC is known as orders of magnitude lower than the electric conductivity of Pt [15]. Therefore, when the lateral dimension of the thin-film fuel cell was small as hundreds of microns or less, the electronic resistance in Pt electrodes could be neglected in the estimation of the ohmic loss. However, while the thickness of membranes remained in hundreds of nanometer-scale, the dimension was largely extended to millimeter-scale in this study. As a result, the ion conducting resistance through the electrolyte membrane became smaller

than the sheet resistance against the lateral electronic conduction. In other words, the larger the electrolyte membrane becomes, the smaller the resistance to the larger flux of ions becomes. It was observed in the polarization and the EIS measurements, that the ohmic loss was governed by the sheet resistance. That is, the electronic resistance is no longer negligible in the case of scaled up thin-film SOFCs.

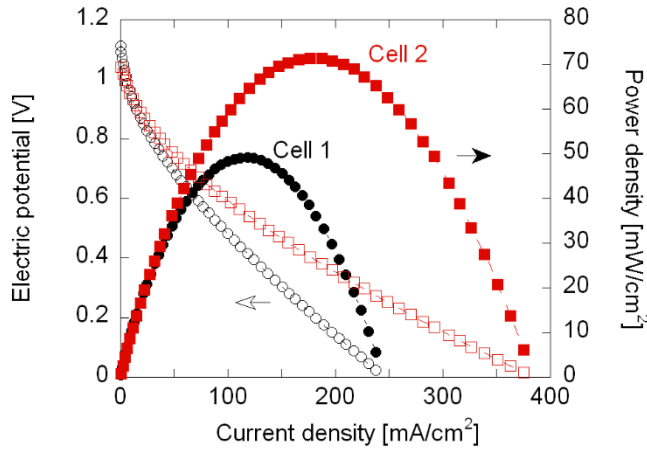


Figure 4.4 Current density–voltage curves of cell 1 and 2

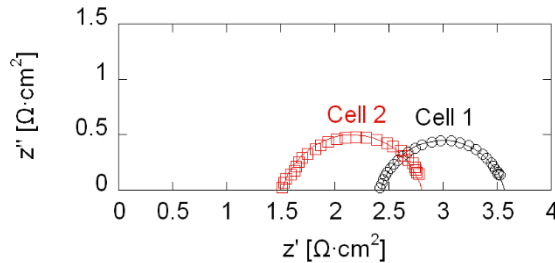


Figure 4.5 Electrochemical impedance spectra of cell 1 and 2

To investigate the effect of the sheet resistance on the thin-film SOFCs that have larger active areas, the Pt thin films of 200 nm thickness were prepared by DC sputtering on the silicon oxide wafer, with variance of the Ar pressure from 5 mTorr to 90 mTorr. The sheet resistance values measured by four-point probe measurements from the prepared Pt films are shown in Figure 4.6. As the sputtering pressure increased, the sheet resistance of the sputtered Pt film increased. The morphology of the metallic electrode being denser, it seems to have a better electrical connection, as also shown in Figure 4.3. These results show that the in-plane conduction of electron in the electrode can become more dominant than the through-plane conduction of ion in the electrolyte membrane, as the scaling up of the cell area causes the sheet resistance effect of the thin electrode layer. Moreover, the increased sheet resistance effect can make the ohmic loss more rate-controlling than the concentration loss in the electrochemical polarization of the fuel cells. Consequently, it is more favorable to apply less porous cathode layers in dealing with thin-film SOFCs with larger active areas.



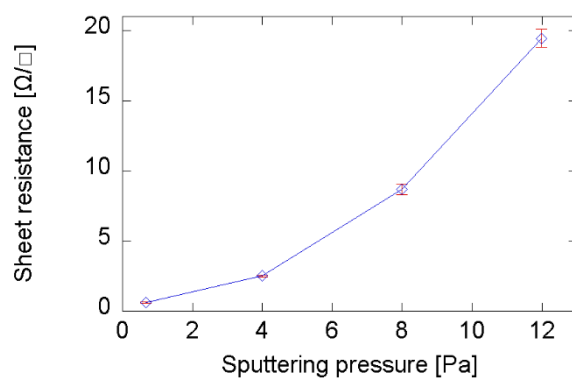


Figure 4.6 Sheet resistance of the Pt thin films with variance of the sputtering pressure

### 4.3.3 Improvement of Current Collection

The previous results show that the in-plane conduction of electron in the electrode can become more dominant than the through-plane conduction of ion in the electrolyte membrane, as the scaling up of the cell area causes the sheet resistance effect of the thin electrode layer. Moreover, the increased sheet resistance effect can make the ohmic loss more rate-controlling than the concentration loss in the electrochemical polarization of the fuel cells. Consequently, it is more favorable to apply less porous cathode layers in dealing with thin-film SOFCs with larger active areas.

Although the ohmic resistance value of cell 2 was fairly smaller than that of cell 1, it still contributed to a major part of the voltage drop. The ohmic loss caused by the oxygen ion conduction through the 750 nm electrolyte is expected to be less than  $0.1 \Omega \cdot \text{cm}^2$  referring to the earlier measurements regarding the conductivities of YSZ and GDC at 500 °C [15], [38], [39]. Therefore, the additional structure, which improves the electronic conduction to the cathode layer, can further enhance the overall electrochemical performance.

Because the cross patterned Pt structure of cell 3 were sputtered at 5 mTorr, it provided a highly conductive path for

the electrons owing to its lower sheet resistance as shown in Figure 4.6. The polarization curve of cell 3 depicted in Figure 4.7 indicates the peak power density was enhanced to approximately  $100 \text{ mW/cm}^2$ . As a result, the total power output from a  $25 \text{ mm}^2$  single fuel cell was about 25 mW.

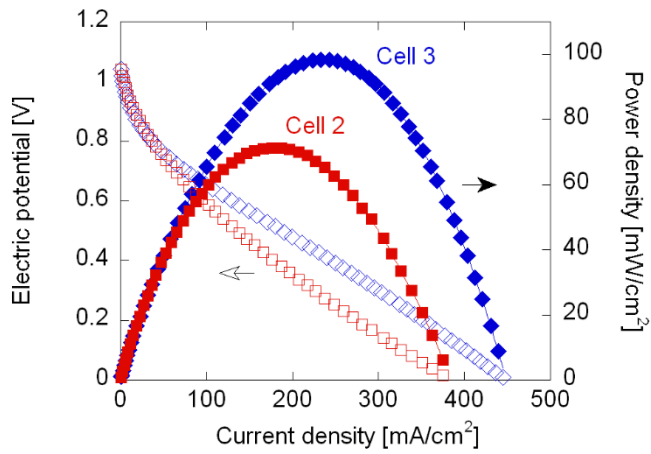


Figure 4.7 Current density–voltage curves of cell 2 and 3

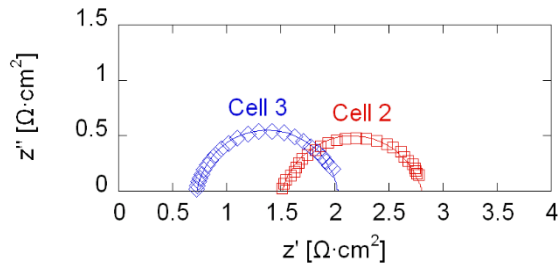


Figure 4.8 Electrochemical impedance spectra of cell 2 and 3

As shown in the Nyquist plot of cell 3 in Figure 4.8, its ohmic resistance was about  $0.72\ \Omega\cdot\text{cm}^2$ , which is even less than half the ohmic resistance of the cell 2. Furthermore, the faradaic resistance was about  $1.31\ \Omega\cdot\text{cm}^2$ , meaning that there was no significant increase of the activation and concentration overpotential caused by the dense Pt pattern on the cathode layer. This result implies that the optimization with the use of the current-collecting structure can minimize the sheet resistance, and consequently improve the electrochemical performance of the enlarged thin-film SOFCs.

## 4.4 Conclusion

In this study, it was verified that the thin-film fuel cell supported by the AAO can be successfully scaled up to 25 mm<sup>2</sup> of active area. The OCV values were close to the theoretically expected value, which indicates that the cells were mechanically stabled in spite of the extremely high aspect ratio of the cross sectional geometry. The effect of the cathode morphology on the ohmic and the faradaic resistance and how the sheet resistance works in the enlarged thin film fuel cells were discussed.

Moreover, it was shown that the additional current-collecting path was able to enhance the lateral electron conduction effectively. It is suggested that the total power output of the thin-film SOFCs at lower temperatures can be increased enough to be applied in practical use.

To further enhance the cell performance, it is required not only to optimize the electrode structures and the current-collector, but also improve the electrochemical kinetics, considering that the ohmic and the faradaic resistances are closely interrelated. Therefore, it is desirable that future researches on the scaling up of the thin-film fuel cells be conducted along with understanding of the nanoscale electrochemical properties.

## CHAPTER 5      CONCLUDING REMARKS

### 5.1 Summary

The effects of the anode microstructure on the fuel cell performance were mainly investigated in this study. In the AAO based thin-film fuel cells, the sputtering atmosphere and the sputtering time had a significant effect on the morphology of the electrode including the distribution of the TPBs and the pores. The OCVs were close to the theoretical value calculated by Nernst equation even in the cells with the more porous anodes. The thicker anode deposited at lower sputtering pressure indicated a higher concentration overpotential. In terms of activation overpotential, the more porous anode structures were more favorable, due to the higher TPB densities than the denser anodes.

The nano-thin YSZ membranes by ALD and sputtering were also examined to figure out the effects of the electrolyte deposition techniques on the performance of the thin-film SOFCs supported by the AAO substrate. The nano-granular morphology and the amorphous crystalline phase of the ALD YSZ improved the electrochemical reactivity of the fuel cell, as found in previous researches on thin-film SOFCs with other structures. Furthermore, the results of the galvanostatic

measurements indicated that the long-term stability of the cells on the AAO could also be enhanced by applying the ALD YSZ thin-film to moderate the degradation of the porous cathode. Lastly, the scaling up of the thin-film fuel cells based on the AAO template was demonstrated in this study. The active area of a single cell was enlarged to 25 mm<sup>2</sup>, which is the largest in micro SOFCs with nano-thin MEAs so far. Moreover, it was revealed that when the active area is enlarged, the sheet resistance of the porous thin-film electrode can be a major factor of the ohmic resistance of the fuel cell rather than the electrolyte resistance.

## 5.2 Future Works

This study underlines the possibility of the thin-film structure based on the AAO substrate for scaling up of the intermediate temperature SOFCs. For commercial usage of the thin-film SOFCs, however, a further improvement in the fuel cell performance is still required. It was shown that the porous anode structures could improve the fuel cell performance by reducing the activation and the concentration overpotentials. Therefore, optimization of the anode microstructures can further enhance the fuel cell performance. In addition, the effects of properties of the templates such as porosity and pore size on the anode microstructure should be investigated. As the lateral dimension is enlarged by order of 4 times larger than the thickness of the electrodes, the lateral conduction of electrons in the electrodes became one of the major factors of the fuel cell performance. The sheet resistance problems in the porous, nano-thin electrodes can be mitigated by improving the current collection of the thin-film fuel cells. It has been reported that a micro metal grid fabricated by MEMS techniques successfully worked as a current collector in thin-film SOFCs. Consequently, optimizing the electronic conduction in the electrodes by applying such new techniques will lead to an increase of the total power output of the fuel cell, finally accelerating the



commercialization of the thin-film SOFC systems.

## REFERENCES

- [1] A. Atkinson, S. Barnett, R. J. Gorte, J. T. S. Irvine, A. J. McEvoy, M. Mogensen, S. C. Singhal, and J. Vohs, "Advanced anodes for high-temperature fuel cells.," *Nat. Mater.*, vol. 3, no. 1, pp. 17-27, Jan. 2004.
- [2] B. C. Steele and A. Heinzl, "Materials for fuel-cell technologies.," *Nature*, vol. 414, no. 6861, pp. 345-52, Nov. 2001.
- [3] S. M. Haile, "Materials for fuel cells," *Membr. Technol.*, vol. 6, no. 3, pp. 24-29, 2003.
- [4] I. Chang, S. Ha, J. Kim, J. Lee, and S. W. Cha, "Performance evaluation of passive direct methanol fuel cell with methanol vapour supplied through a flow channel," *J. Power Sources*, vol. 184, no. 1, pp. 9-15, Sep. 2008.
- [5] I. Chang, S. Ha, S. Kim, S. Kang, J. Kim, K. Choi, and S. W. Cha, "Operational condition analysis for vapor-fed direct methanol fuel cells," *J. Power Sources*, vol. 188, no. 1, pp. 205-212, Mar. 2009.
- [6] I. Chang, M. Lee, and S. W. Cha, "Characteristic behaviors on air-breathing direct methanol fuel cells," *Int. J. Precis. Eng. Manuf.*, vol. 13, no. 7, pp. 1141-1144, Jul. 2012.
- [7] Y. H. Lee, T. Park, I. Chang, S. Ji, and S. W. Cha, "Metal-coated polycarbonate monopolar plates for portable fuel cells," *Int. J. Hydrogen Energy*, vol. 37, no. 23, pp. 18471-18475, Dec. 2012.
- [8] I. Chang, M. H. Lee, J.-H. Lee, Y.-S. Kim, and S. W. Cha, "Air-breathing flexible Polydimethylsiloxane (PDMS) -

- based fuel cell,” *Int. J. Precis. Eng. Manuf.*, vol. 14, no. 3, pp. 501–504, Mar. 2013.
- [9] T. Park, I. Chang, Y. H. Lee, S. Ji, and S. W. Cha, “Analysis of operational characteristics of polymer electrolyte fuel cell with expanded graphite flow–field plates via electrochemical impedance investigation,” *Energy*, vol. 66, pp. 77–81, Mar. 2014.
  - [10] Z. Shao and S. M. Haile, “A high–performance cathode for the next generation of solid–oxide fuel cells.,” *Nature*, vol. 431, no. 7005, pp. 170–3, Sep. 2004.
  - [11] D. Beckel, U. P. Muecke, T. Gyger, G. Florey, A. Infortuna, and L. J. Gauckler, “Electrochemical performance of LSCF based thin film cathodes prepared by spray pyrolysis,” *Solid State Ionics*, vol. 178, no. 5–6, pp. 407–415, 2007.
  - [12] I. Chang, T. Park, J. Lee, M. H. Lee, S. H. Ko, and S. W. Cha, “Bendable polymer electrolyte fuel cell using highly flexible Ag nanowire percolation network current collectors,” *J. Mater. Chem. A*, vol. 1, no. 207890, p. 8541, 2013.
  - [13] R. O’Hayre, S. Cha, W. Colella, and F. Prinz, *Fuel cell fundamentals*. New York: John Wiley & Sons, 2006.
  - [14] S. C. Singhal and K. Kendall, *High–temperature solid oxide fuel cells: fundamentals, design and applications: fundamentals, design and applications*. Elsevier, 2003.
  - [15] S. M. Haile, “Fuel cell materials and components,” *Acta Mater.*, vol. 51, no. 19, pp. 5981–6000, Nov. 2003.
  - [16] H. Y. Jung, K.–S. Hong, H. Kim, J.–K. Park, J.–W. Son, J. Kim, H.–W. Lee, and J.–H. Lee, “Characterization of Thin–Film YSZ Deposited via EB–PVD Technique in Anode–supported SOFCs,” *J. Electrochem. Soc.*, vol. 153, no. 6, p. A961, 2006.

- [17] D. Beckel, a. Bieberle–Hütter, a. Harvey, a. Infortuna, U. P. Muecke, M. Prestat, J. L. M. Rupp, and L. J. Gauckler, “Thin films for micro solid oxide fuel cells,” *J. Power Sources*, vol. 173, no. 1, pp. 325–345, 2007.
- [18] A. Infortuna, A. S. Harvey, and L. J. Gauckler, “Microstructures of CGO and YSZ thin films by pulsed laser deposition,” *Adv. Funct. Mater.*, vol. 18, no. 1, pp. 127–135, 2008.
- [19] S. Heiroth, T. Lippert, a. Wokaun, M. Döbeli, J. L. M. Rupp, B. Scherrer, and L. J. Gauckler, “Ytria–stabilized zirconia thin films by pulsed laser deposition: Microstructural and compositional control,” *J. Eur. Ceram. Soc.*, vol. 30, no. 2, pp. 489–495, 2010.
- [20] U. P. Muecke, D. Beckel, A. Bernard, A. Bieberle–Hütter, S. Graf, A. Infortuna, P. Müller, J. L. M. Rupp, J. Schneider, and L. J. Gauckler, “Micro solid oxide fuel cells on glass ceramic substrates,” *Adv. Funct. Mater.*, vol. 18, no. 20, pp. 3158–3168, 2008.
- [21] J. H. Shim, J. S. Park, J. An, T. M. Gür, S. Kang, and F. B. Prinz, “Intermediate–temperature ceramic fuel cells with thin film yttrium–doped barium zirconate electrolytes,” *Chem. Mater.*, vol. 21, no. 14, pp. 3290–3296, 2009.
- [22] H. S. Noh, J. S. Park, J. W. Son, H. Lee, J. H. Lee, and H. W. Lee, “Physical and microstructural properties of NiO– and Ni–YSZ composite thin films fabricated by pulsed–laser deposition at T???700??C,” *J. Am. Ceram. Soc.*, vol. 92, no. 12, pp. 3059–3064, 2009.
- [23] H.–S. Noh, J.–W. Son, H. Lee, H.–S. Song, H.–W. Lee, and J.–H. Lee, “Low Temperature Performance Improvement of SOFC with Thin Film Electrolyte and Electrodes Fabricated by Pulsed Laser Deposition,” *J. Electrochem. Soc.*, vol. 156, no. 12, p. B1484, 2009.

- [24] S. M. Kim, J. W. Son, K. R. Lee, H. Kim, H. R. Kim, H. W. Lee, and J. H. Lee, "Substrate effect on the electrical properties of sputtered YSZ thin films for co-planar SOFC applications," *J. Electroceramics*, vol. 24, no. 3, pp. 153–160, 2010.
- [25] J. L. M. Rupp, U. P. Muecke, P. C. Nalam, and L. J. Gauckler, "Wet-etching of precipitation-based thin film microstructures for micro-solid oxide fuel cells," *J. Power Sources*, vol. 195, no. 9, pp. 2669–2676, 2010.
- [26] T. Ryll, A. Brunner, S. Ellenbroek, A. Bieberle-Hutter, J. L. M. Rupp, and L. J. Gauckler, "Electrical conductivity and crystallization of amorphous bismuth ruthenate thin films deposited by spray pyrolysis.," *Phys. Chem. Chem. Phys.*, vol. 12, no. 42, pp. 13933–13942, 2010.
- [27] Y. Takagi, B.-K. Lai, K. Kerman, and S. Ramanathan, "Low temperature thin film solid oxide fuel cells with nanoporous ruthenium anodes for direct methane operation," *Energy Environ. Sci.*, vol. 4, no. 9, p. 3473, 2011.
- [28] Y. B. Kim, J. S. Park, T. M. Gür, and F. B. Prinz, "Oxygen activation over engineered surface grains on YDC/YSZ interlayered composite electrolyte for LT-SOFC," *J. Power Sources*, vol. 196, no. 24, pp. 10550–10555, 2011.
- [29] Y. B. Kim, J. H. Shim, T. M. Gür, and F. B. Prinz, "Epitaxial and Polycrystalline Gadolinia-Doped Ceria Cathode Interlayers for Low Temperature Solid Oxide Fuel Cells," *J. Electrochem. Soc.*, vol. 158, no. 11, p. B1453, 2011.
- [30] E. D. Wachsman and K. T. Lee, "Lowering the temperature of solid oxide fuel cells.," *Science*, vol. 334, no. 6058, pp. 935–9, Nov. 2011.

- [31] P. C. Su and F. B. Prinz, "Nanoscale membrane electrolyte array for solid oxide fuel cells," *Electrochem. commun.*, vol. 16, no. 1, pp. 77–79, 2012.
- [32] K. Bae, D. Y. Jang, H. J. Jung, J. W. Kim, J. W. Son, and J. H. Shim, "Micro ceramic fuel cells with multilayered yttrium–doped barium cerate and zirconate thin film electrolytes," *J. Power Sources*, vol. 248, pp. 1163–1169, 2014.
- [33] J. Fleig, H. L. Tuller, and J. Maier, "Electrodes and electrolytes in micro–SOFCs: A discussion of geometrical constraints," *Solid State Ionics*, vol. 174, no. 1–4, pp. 261–270, 2004.
- [34] S. Kang, P. Heo, Y. H. Lee, J. Ha, I. Chang, and S.–W. Cha, "Low intermediate temperature ceramic fuel cell with Y–doped BaZrO<sub>3</sub> electrolyte and thin film Pd anode on porous substrate," *Electrochem. commun.*, vol. 13, no. 4, pp. 374–377, Apr. 2011.
- [35] C. Brahim, A. Ringuedé, E. Gourba, M. Cassir, A. Billard, and P. Briois, "Electrical properties of thin bilayered YSZ/GDC SOFC electrolyte elaborated by sputtering," *J. Power Sources*, vol. 156, no. 1, pp. 45–49, May 2006.
- [36] S. H. Choi, S. W. Kim, C. S. Hwang, and M. H. Lee, "Freestanding Micro–SOFCs with Electrodes Prepared by Electrostatic Spray Deposition," *Fuel Cells*, vol. 14, no. 2, pp. 332–335, 2014.
- [37] S. H. Choi, C. S. Hwang, and M. H. Lee, "Performance Enhancement of Freestanding Micro–SOFCs with Ceramic Electrodes by the Insertion of a YSZ–Ag Interlayer," *ECS Electrochem. Lett.*, vol. 3, no. 9, pp. F57–F59, 2014.
- [38] H. Huang, M. Nakamura, P. Su, R. Fasching, Y. Saito, and F. B. Prinz, "High–Performance Ultrathin Solid Oxide

- Fuel Cells for Low-Temperature Operation,” *J. Electrochem. Soc.*, vol. 154, no. 1, p. B20, 2007.
- [39] J. H. Shim, C. C. Chao, H. Huango, and F. B. Prinz, “Atomic layer deposition of yttria-stabilized zirconia for solid oxide fuel cells,” *Chem. Mater.*, vol. 19, no. 7, pp. 3850–3854, 2007.
- [40] H. Huang, J. H. Shim, C.-C. Chao, R. Pornprasertsuk, M. Sugawara, T. M. Gu“ r, and F. B. Prinz, “Characteristics of Oxygen Reduction on Nanocrystalline YSZ,” *J. Electrochem. Soc.*, vol. 156, no. 3, p. B392, 2009.
- [41] P. C. Su, C. C. Chao, J. H. Shim, R. Fasching, and F. B. Prinz, “Solid oxide fuel cell with corrugated thin film electrolyte,” *Nano Lett.*, vol. 8, no. 100, pp. 2289–2292, 2008.
- [42] C.-C. Chao, C.-M. Hsu, Y. Cui, and F. B. Prinz, “Improved Solid Oxide Fuel Cell Performance with Nanostructured Electrolytes,” *ACS Nano*, vol. 5, no. 7, pp. 5692–5696, Jul. 2011.
- [43] J. JOO and G. CHOI, “Open-circuit voltage of ceria-based thin film SOFC supported on nano-porous alumina,” *Solid State Ionics*, vol. 178, no. 29–30, pp. 1602–1607, Dec. 2007.
- [44] S. Kang, P. C. Su, Y. I. Park, Y. Saito, and F. B. Prinz, “Thin-Film Solid Oxide Fuel Cells on Porous Nickel Substrates with Multistage Nanohole Array,” *J. Electrochem. Soc.*, vol. 153, no. 3, p. A554, 2006.
- [45] J. Park, J. Y. Paek, I. Chang, S. Ji, S. W. Cha, and S. I. Oh, “Pulsed laser deposition of Y-doped BaZrO<sub>3</sub> thin film as electrolyte for low temperature solid oxide fuel cells,” *CIRP Ann. – Manuf. Technol.*, vol. 62, no. 1, pp. 563–566, 2013.

- [46] C.-W. Kwon, J.-W. Son, J.-H. Lee, H.-M. Kim, H.-W. Lee, and K.-B. Kim, "High-Performance Micro-Solid Oxide Fuel Cells Fabricated on Nanoporous Anodic Aluminum Oxide Templates," *Adv. Funct. Mater.*, vol. 21, no. 6, pp. 1154-1159, Mar. 2011.
- [47] S. Ha, P.-C. Su, and S.-W. Cha, "Combinatorial deposition of a dense nano-thin film YSZ electrolyte for low temperature solid oxide fuel cells," *J. Mater. Chem. A*, vol. 1, no. 207890, p. 9645, 2013.
- [48] S. Ji, I. Chang, Y. H. Lee, J. Park, J. Y. Paek, M. H. Lee, and S. W. Cha, "Fabrication of low-temperature solid oxide fuel cells with a nanothin protective layer by atomic layer deposition.," *Nanoscale Res. Lett.*, vol. 8, no. 1, p. 48, Jan. 2013.
- [49] A. C. Johnson, A. Baclig, D. V. Harburg, B. K. Lai, and S. Ramanathan, "Fabrication and electrochemical performance of thin-film solid oxide fuel cells with large area nanostructured membranes," *J. Power Sources*, vol. 195, no. 4, pp. 1149-1155, 2010.
- [50] M. Tsuchiya, B.-K. Lai, and S. Ramanathan, "Scalable nanostructured membranes for solid-oxide fuel cells.," *Nat. Nanotechnol.*, vol. 6, no. 5, pp. 282-286, 2011.
- [51] S. Ji, I. Chang, G. Y. Cho, Y. H. Lee, J. H. Shim, and S. W. Cha, "Application of dense nano-thin platinum films for low-temperature solid oxide fuel cells by atomic layer deposition," *Int. J. Hydrogen Energy*, vol. 39, no. 23, pp. 12402-12408, Aug. 2014.
- [52] S. Ji, I. Chang, Y. H. Lee, M. H. Lee, and S. W. Cha, "Performance enhancement of thin-film ceramic electrolyte fuel cell using bi-layered yttrium-doped barium zirconate," *Thin Solid Films*, vol. 539, pp. 117-121, Jul. 2013.



- [53] I. Chang, P. Heo, and S. W. Cha, "Thin film solid oxide fuel cell using a pinhole-free and dense Y-doped BaZrO<sub>3</sub>," *Thin Solid Films*, vol. 534, pp. 286–290, May 2013.
- [54] C.-W. Kwon, J.-I. Lee, K.-B. Kim, H.-W. Lee, J.-H. Lee, and J.-W. Son, "The thermomechanical stability of micro-solid oxide fuel cells fabricated on anodized aluminum oxide membranes," *J. Power Sources*, vol. 210, pp. 178–183, Jul. 2012.
- [55] J. Park, Y. Lee, I. Chang, W. Lee, and S. W. Cha, "Engineering of the electrode structure of thin film solid oxide fuel cells," *Thin Solid Films*, Nov. 2014.
- [56] J. Park, I. Chang, J. Y. Paek, S. Ji, W. Lee, S. W. Cha, and J. M. Lee, "Fabrication of the large area thin-film solid oxide fuel cells," *CIRP Ann. – Manuf. Technol.*, vol. 63, no. 1, pp. 513–516, 2014.
- [57] T. P. Holme, R. Pornprasertsuk, and F. B. Prinz, "Interpretation of Low Temperature Solid Oxide Fuel Cell Electrochemical Impedance Spectra," *J. Electrochem. Soc.*, vol. 157, no. 1, p. B64, 2010.
- [58] J. H. Shim, J. S. Park, T. P. Holme, K. Crabb, W. Lee, Y. B. Kim, X. Tian, T. M. Gür, and F. B. Prinz, "Enhanced oxygen exchange and incorporation at surface grain boundaries on an oxide ion conductor," *Acta Mater.*, vol. 60, no. 1, pp. 1–7, 2012.
- [59] Z. Fan and F. B. Prinz, "Enhancing oxide ion incorporation kinetics by nanoscale Yttria-doped ceria interlayers," *Nano Lett.*, vol. 11, no. 6, pp. 2202–2205, 2011.
- [60] J. An, Y. B. Kim, J. S. Park, T. M. Gür, and F. B. Prinz, "Three-dimensional nanostructured bilayer solid oxide fuel cell with 1.3 W/cm<sup>2</sup> at 450° C," *Nano Lett.*, 2013.

- [61] A. C. Johnson, B. K. Lai, H. Xiong, and S. Ramanathan, "An experimental investigation into micro-fabricated solid oxide fuel cells with ultra-thin  $\text{La}_{0.6}\text{Sr}_{0.4}\text{Co}_{0.8}\text{Fe}_{0.2}\text{O}_3$  cathodes and yttria-doped zirconia electrolyte films," *J. Power Sources*, vol. 186, no. 2, pp. 252–260, 2009.
- [62] Y. B. Kim, T. M. Gür, S. Kang, H. J. Jung, R. Sinclair, and F. B. Prinz, "Crater patterned 3-D proton conducting ceramic fuel cell architecture with ultra thin Y:BaZrO<sub>3</sub> electrolyte," *Electrochem. commun.*, vol. 13, no. 5, pp. 403–406, 2011.
- [63] E.-O. Oh, C.-M. Whang, Y.-R. Lee, S.-Y. Park, D. H. Prasad, K. J. Yoon, J.-W. Son, J.-H. Lee, and H.-W. Lee, "Extremely thin bilayer electrolyte for solid oxide fuel cells (SOFCs) fabricated by chemical solution deposition (CSD).," *Adv. Mater.*, vol. 24, no. 25, pp. 3373–7, Jul. 2012.
- [64] K. Kerman, B. K. Lai, and S. Ramanathan, "Pt/Y<sub>0.16</sub>Zr<sub>0.84</sub>O<sub>1.92</sub>/Pt thin film solid oxide fuel cells: Electrode microstructure and stability considerations," *J. Power Sources*, vol. 196, no. 5, pp. 2608–2614, 2011.
- [65] D. Perednis and L. J. Gauckler, "Solid oxide fuel cells with electrolytes prepared via spray pyrolysis," *Solid State Ionics*, vol. 166, no. 3–4, pp. 229–239, 2004.
- [66] J. L. M. Rupp, T. Drobek, A. Rossi, and L. J. Gauckler, "Chemical analysis of spray pyrolysis gadolinia-doped ceria electrolyte thin films for solid oxide fuel cells," *Chem. Mater.*, vol. 19, no. 5, pp. 1134–1142, 2007.
- [67] J. Y. Paek, I. Chang, J. H. Park, S. Ji, and S. W. Cha, "A study on properties of yttrium-stabilized zirconia thin films fabricated by different deposition techniques," *Renew. Energy*, vol. 65, pp. 202–206, May 2014.

- [68] I. Chang, J. Y. Paek, and S. W. Cha, "Parametric study of Y-doped BaZrO<sub>3</sub> thin film deposited via pulsed laser deposition," *J. Vac. Sci. Technol. A Vacuum, Surfaces, Film.*, vol. 33, no. 2, p. 021515, Mar. 2015.
- [69] H. S. Noh, J. W. Son, H. Lee, H. Il Ji, J. H. Lee, and H. W. Lee, "Suppression of Ni agglomeration in PLD fabricated Ni-YSZ composite for surface modification of SOFC anode," *J. Eur. Ceram. Soc.*, vol. 30, no. 16, pp. 3415-3423, 2010.
- [70] H.-S. Noh, H. Lee, H.-I. Ji, H.-W. Lee, J.-H. Lee, and J.-W. Son, "Limitation of Thickness Increment of Lanthanum Strontium Cobaltite Cathode Fabricated by Pulsed Laser Deposition," *J. Electrochem. Soc.*, vol. 158, no. 1, p. B1, 2011.
- [71] W. Lee, H. J. Jung, M. H. Lee, Y. B. Kim, J. S. Park, R. Sinclair, and F. B. Prinz, "Oxygen Surface Exchange at Grain Boundaries of Oxide Ion Conductors," *Adv. Funct. Mater.*, vol. 22, pp. 965-971, 2012.
- [72] C.-C. Chao, Y. B. Kim, and F. B. Prinz, "Surface modification of yttria-stabilized zirconia electrolyte by atomic layer deposition," *Nano Lett.*, vol. 9, no. 10, pp. 3626-3628, 2009.
- [73] C. C. Chao, J. S. Park, X. Tian, J. H. Shim, T. M. Gür, and F. B. Prinz, "Enhanced oxygen exchange on surface-engineered yttria-stabilized zirconia," *ACS Nano*, vol. 7, pp. 2186-2191, 2013.
- [74] T. Ryll, H. Galinski, L. Schlagenhauf, P. Elser, J. L. M. Rupp, A. Bieberle-Hutter, and L. J. Gauckler, "Microscopic and nanoscopic three-phase-boundaries of platinum thin-film electrodes on YSZ electrolyte," *Adv. Funct. Mater.*, vol. 21, no. 3, pp. 565-572, 2011.
- [75] Y. B. Kim, C.-M. Hsu, S. T. Connor, T. M. Gür, Y. Cui, and F. B. Prinz, "Nanopore Patterned Pt Array Electrodes

for Triple Phase Boundary Study in Low Temperature SOFC,” *J. Electrochem. Soc.*, vol. 157, no. 9, p. B1269, 2010.

- [76] E. Jiran and C. V. Thompson, “Capillary instabilities in thin, continuous films,” *Thin Solid Films*, vol. 208, no. 1, pp. 23–28, Feb. 1992.
- [77] E. Jiran and C. V. Thompson, “Capillary instabilities in thin films,” *J. Electron. Mater.*, vol. 19, no. 11, pp. 1153–1160, Nov. 1990.
- [78] C. V. Thompson, “Solid–State Dewetting of Thin Films,” *Annu. Rev. Mater. Res.*, vol. 42, no. 1, pp. 399–434, 2012.
- [79] K. Kerman, B. K. Lai, and S. Ramanathan, “Thin film nanocrystalline  $\text{Ba}_{0.5}\text{Sr}_{0.5}\text{Co}_{0.8}\text{Fe}_{0.2}\text{O}_3$ : Synthesis, conductivity, and micro–solid oxide fuel cells,” *J. Power Sources*, vol. 196, no. 15, pp. 6214–6218, 2011.
- [80] B. K. Lai, K. Kerman, and S. Ramanathan, “On the role of ultra–thin oxide cathode synthesis on the functionality of micro–solid oxide fuel cells: Structure, stress engineering and in situ observation of fuel cell membranes during operation,” *J. Power Sources*, vol. 195, no. 16, pp. 5185–5196, 2010.
- [81] B. K. Lai, K. Kerman, and S. Ramanathan, “Methane–fueled thin film micro–solid oxide fuel cells with nanoporous palladium anodes,” *J. Power Sources*, vol. 196, no. 15, pp. 6299–6304, 2011.
- [82] I. Chang, S. Woo, M. H. Lee, J. H. Shim, Y. Piao, and S. W. Cha, “Characterization of porous Pt films deposited via sputtering,” *Appl. Surf. Sci.*, vol. 282, pp. 463–466, Oct. 2013.

## 국문 초록

중저온형 박막 연료전지는 500 °C 이하의 작동 온도에서도 높은 에너지 밀도를 가지는 장점 때문에 새로운 개념의 연료전지 시스템으로서 많은 관심을 받아왔다. 또한 마이크로/나노미터 수준의 제조 공정 및 분석 기술의 발달은 박막 연료전지의 구조에 대한 다양하고 창의적인 접근 방법들을 가능하게 하였다. 한편, 수십/수백 나노미터 박막의 구조적 한계 때문에 박막 연료전지를 지지하기 위해 다공성 기판을 이용하는 연구들이 시도되었다.

연료전지 작동 시 발생하는 활성화 과전압에서 수소 산화 반응에 비해 공기극에서의 산소 환원 반응에 의한 손실이 많은 비중을 차지하기 때문에, 박막 연료전지에 대한 많은 연구들은 연료극보다는 공기극 설계나 공기극과 전해질의 계면 개선에 집중되어 있다. 그러나, 다공성 지지체 기반 박막 연료전지에서는 연료극이 기판의 나노 기공 배열 위에 형성되기 때문에 증착 조건에 따른 전극 구조 특성과 이러한 특성이 연료전지 성능에 미치는 영향을 살펴볼 필요가 있다. 본 연구에서는 연료극 구조가 전해질-전극의 삼상 계면과 전극 내 기공도를 결정함으로써 연료전지의 전기화학 반응성과 물질 전달 특성에 지대한 영향을 미칠 수 있음을 확인하였다.

다공성 지지체 기반 박막 연료전지 분야의 초기 연구들은 기판의 기공에서 과생되는 전해질 내 미세 결함을 방지하기 위해 많은 노력을 기울였다. 그 결과, 최근 박막 전해질 제작에 원자층 증착법 (atomic layer deposition, ALD)을 적용하여 1 V 이상의 개회로 전

압 (open circuit voltage, OCV) 값을 얻은 결과들이 보고되었다. 원자층 증착법을 통해 제작된 이트리아 안정화 지르코니아 (yttria stabilized zirconia) 전해질 박막은 전통적인 방식에 의한 것보다 향상된 전기화학적 특성을 보이는 것으로 알려져 있다. 본 연구에서는 스퍼터링과 ALD 기법을 YSZ 전해질 증착에 적용하여 다공성 지지체 기반 박막 연료전지를 제작하고, 그 특성들을 비교 분석하였다. 전기화학적 성능 평가 결과, ALD 공정을 통해 증착된 YSZ 전해질은 스퍼터된 박막에 비해 연료전지 출력 밀도를 두 배 이상 향상시키고, 450 °C에서 공기극의 열화 현상을 경감시켜 다공성 기판 기반 박막 연료전지의 내구성을 크게 개선하는 효과가 있음을 확인하였다.

다공성 지지체 기반 구조는 박막의 열/기계적 안정성을 보완하여 중저온형 연료전지의 대면적화 및 전체 출력의 향상을 위해 제안되었다. 본 연구에서는 다공성 기판 및 박막 공정을 적용하여 25 mm<sup>2</sup>의 면적을 가지는 박막 연료전지를 성공적으로 구현하였으며, 이는 다공성 지지체 기반 구조를 통한 대면적 박막 연료전지의 가능성을 처음으로 실증한 것이다. 현재까지 전해질-전극 접합체의 총 두께가 수 마이크로미터 이하인 박막 연료전지 중에서는 이보다 넓은 면적을 가지는 결과는 보고되지 않았다. 또한 연료전지 성능 평가 결과, 박막 전극의 대면적화에 따른 추가적인 저항 손실이 있었음에도 불구하고 단일 전지에서 약 25 mW의 전체 출력을 확인하였다. 이는 Tsuchiya 등이 발표한 21.1 mW (13.5 mm<sup>2</sup>의 활성 면적)보다 약 18.5 % 향상된 값이다.

본 연구는 다공성 지지체 기반 박막 연료전지의 연료극 구조 설계와 전해질 증착 공정이 연료전지의 출력 성능 및 내구성에 미치는 영향에 대해 다양한 평가/분석 기법들을 이용하여 살펴보았다. 또한, 대면적 박막 연료전지를 구현하고, 연료전지의 전체 출력을 향상시키기 위한 방안을 모색하여 후속 연구에 대한 방향을 제시하였다.